Biomaterials 331 (2026) 124131

Contents lists available at ScienceDirect

Biomaterials

journal homepage: www.elsevier.com/locate/biomaterials

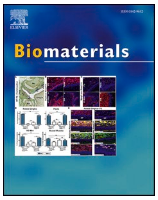

Matrix-guided embryo-like invasion enables 3D heart organoids with atrioventricular synchrony-like contraction

Eun Mi Kim[a], Yujin Ahn[a,b], Jason Wang[c], Joanne Hwang[a], Junggeon Park[a], Kai-Yu Huang[a], Seulgi Kim[d], Sujeong Kim[e], Roy D. Dar[c], Young Jun Kim[f], Heungsoo Shin[g,h,*], Chi Hwan Lee[i,j,k,l,**], Hyunjoon Kong[a,b,c,m,***]

[a] *Department of Chemical and Biomolecular Engineering, University of Illinois at Urbana-Champaign, Urbana, IL, 61801, USA*
[b] *Chan Zuckerberg Biohub Chicago, Chicago, IL, 60642, USA*
[c] *Department of Bioengineering, University of Illinois at Urbana-Champaign, Urbana, IL, 61801, USA*
[d] *School of Chemical Engineering, Sungkyunkwan University, Suwon, 16419, Republic of Korea*
[e] *Department of Immunology, Blavatnik Institute, Harvard Medical School, Boston, MA, 02115, USA*
[f] *Environmental Safety Group, Korea Institute of Science and Technology (KIST) Europe, Saarbrücken, 66123, Germany*
[g] *Department of Bioengineering, Hanyang University, Seoul, 04763, Republic of Korea*
[h] *BK21 FOUR, Education and Research Group for Biopharmaceutical Innovation Leader, Hanyang University, Seoul, 04763, Republic of Korea*
[i] *Weldon School of Biomedical Engineering, Purdue University, West Lafayette, IN, 47907, USA*
[j] *School of Mechanical Engineering, Purdue University, West Lafayette, IN, 47907, USA*
[k] *School of Materials Engineering, Purdue University, West Lafayette, IN, 47907, USA*
[l] *Elmore School of Electrical and Computer Engineering, Purdue University, West Lafayette, IN, 47907, USA*
[m] *Scott H. Fisher Multi-Cellular Engineered Living Systems Theme, Carl R. Woese Institute for Genomic Biology, University of Illinois at Urbana-Champaign, Urbana, IL, 61801, USA*

ARTICLE INFO

Keywords:
Embryoid body
Collagen-poly(ethylene glycol) gel
N-cadherin
Stiffness
Flexible biosensor

ABSTRACT

Engineering heart-like organoids *in vitro* holds significant promise for advancing cardiovascular research. While current approaches, such as suspended cell clusters in media or encapsulating them in gels, have shown potential, they are often challenged in generating organoids with defined chambers and synchronized contractions due to variations in outcomes linked to cell density. In this study, we present a strategy to modulate cell-cell interactions at a fixed cell density by mimicking bioprocesses underlying embryo implantation and invasion. Specifically, an embryoid body cultured on a collagen-poly(ethylene glycol) gel with greater porosity and hydrophilicity and lower stiffness than a pure collagen gel undergoes enhanced invasion and self-organization, resulting in functional, embryo-like cardiac organoids. These organoids exhibit distinct chamber structures surrounded by cardiac muscle, pacemaker cell innervation, atrioventricular synchrony-like contractions, recurring calcium flux, and electrocardiogram-like signals. Organoid development is associated with upregulated expression of mesodermal, ectodermal, and *N*-cadherin genes. This simple yet effective approach will enable robust modeling of heart physiology and drug response *in vitro*, offering valuable insights for translational cardiovascular research.

1. Introduction

The heart, a primary biological pump, is crucial for the circulation of biological molecules and cells. Over the last decades, there have been great advances in understanding and intervening in heart-related diseases. However, cardiovascular disease remains a major cause of death, thus necessitating efforts to develop better medicine and therapeutic interventions. To comply with this effort, engineering heart-like organoids in healthy, injured, and disease states holds significant promise for both fundamental and applied bioscience studies.

---

* Corresponding author. Department of Bioengineering, Hanyang University, Seoul, 04763, Republic of Korea.
** Corresponding author. Weldon School of Biomedical Engineering, Purdue University, West Lafayette, IN, 47907, USA.
*** Corresponding author. Department of Chemical and Biomolecular Engineering, University of Illinois at Urbana-Champaign, Urbana, IL, 61801, USA.
E-mail addresses: hshin@hanyang.ac.kr (H. Shin), lee2270@purdue.edu (C.H. Lee), hjkong06@illinois.edu (H. Kong).

https://doi.org/10.1016/j.biomaterials.2026.124131
Received 30 September 2025; Received in revised form 9 March 2026; Accepted 10 March 2026

It has been common to culture pluripotent stem cell (PSC) clusters in media formulated to activate desired differentiation, because clusters tend to foster a paracrine microenvironment through WNT signaling [1–3]. For instance, PSC aggregates embedded in Matrigel and cultured in the differentiation media were reported to form tissue with a muscle ultrastructure similar to that found in the early native heart [4,5]. Suspending PSCs in media containing laminin-entactin complex and fibroblast growth factor 4 (FGF4) results in a 3D tissue construct exhibiting cardiac tissue-like electrophysiological activation patterns [6]. 3D muscle patch with contraction function was also formed by PSC-derived cardiomyocytes that self-assembled on elastomeric posts [7,8]. Various biofabrication methods, including 3D printing, have also been reported to date [9,10].

These studies suggest that the quality of heart-like organoids is influenced by cell density within stem cell clusters, as higher densities can enhance cell-cell interactions, thereby promoting morphogenesis and functional maturation [4–11]. However, high-density 3D cell clusters may compromise cell viability by limiting mass transport, potentially leading to hypoxia or necrosis at the cluster core. Thus, a more rational design strategy would involve modulating cell-cell interaction without altering cell density to achieve physiologically functional heart organoids [12]. Despite its importance, this approach has not been systematically investigated due to the lack of enabling tools.

To address this gap, we propose a strategy to regulate intercellular emergence at a given cell density by mimicking key biological processes observed during embryo implantation and invasion. *In vivo*, the blastocyst, composed of inner and outer cell masses, adheres to endometrial adhesion receptors and penetrates the basement membrane [13]. This invasion behavior is accompanied by changes in *E*-cadherin and *N*-cadherin expression, which facilitate cell migration and differentiation necessary for tissue development [14]. Furthermore, bioinformatics analysis indicates that gene expression related to cell-cell interactions increases during the early stages of heart development, whereas gene expression associated with focal adhesion decreases (Fig. S1). In contrast, implantation and invasion are impaired in pathological conditions such as uterine fibroids and polyps, where the tissue becomes denser, more hydrophobic, and stiffer, highlighting that the physical properties of the environment critically influence cell behavior [15,16].

We hypothesized that increasing the porosity and hydrophilicity of cell culture substrates, while decreasing their stiffness, would promote the formation of functional, embryo-like heart organoids by enhancing an embryoid body (EB) invasion into the gel, similar to *in vivo* embryoid body invasion, and strengthen cell-cell interaction (Scheme 1). We examined this hypothesis by differentiating a pluripotent EB into cardiomyogenic lineages on collagen-poly(ethylene glycol) (PEG) composite gels. Collagen, which possesses cell-adhesive domains, reproduces the implantation-like adhesion of EBs to the gel [17,18]. By blending PEG into the collagen gel at mass ratios of PEG to collagen

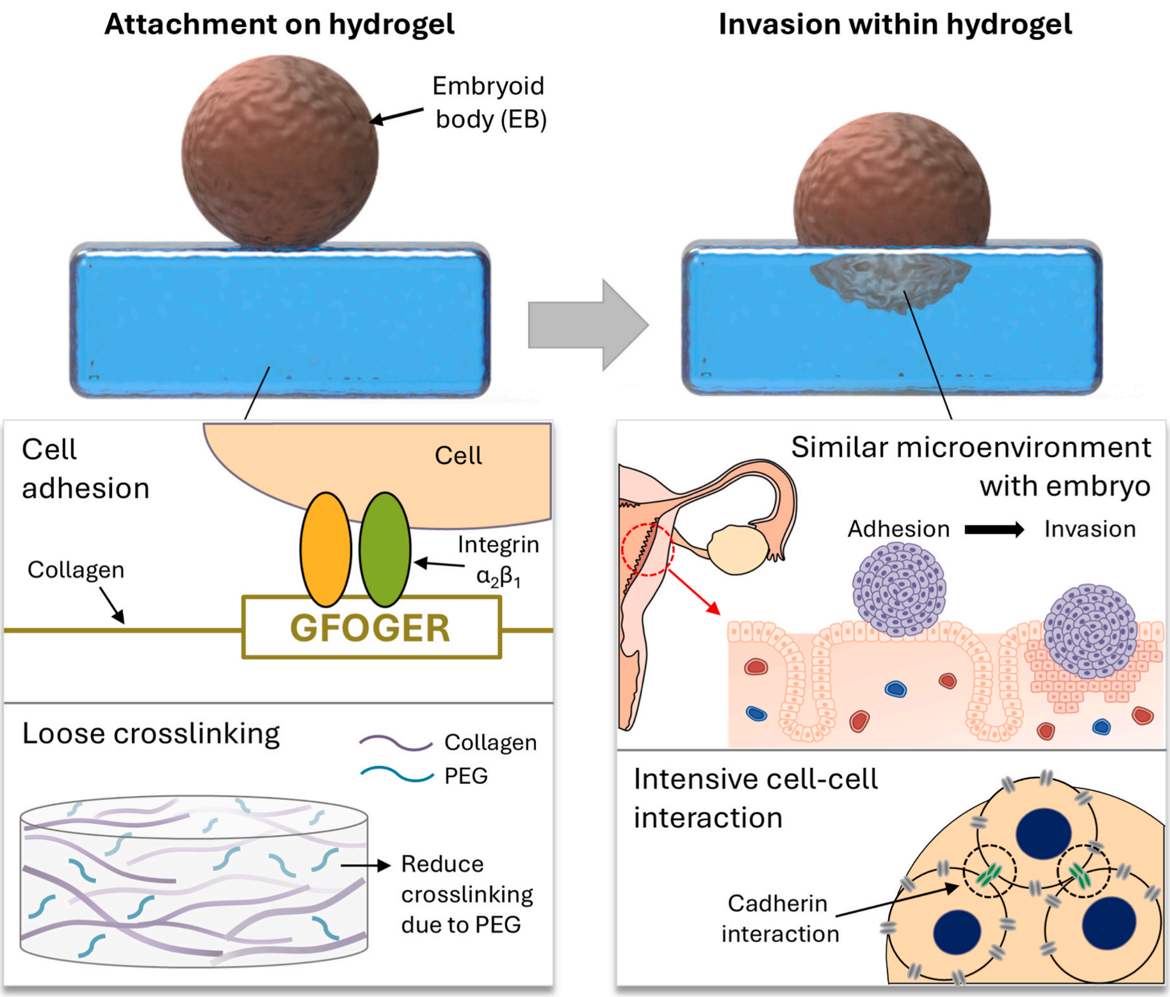

Scheme 1. Schematic illustration of the endometrium-mimicking hydrogel system for cardiac organoid development. The collagen-based hydrogel, with loosely crosslinked fibril networks enhanced by PEG incorporation, enables the embryonic body to invade the hydrogel after plating. This biomimetic environment promotes robust cell-cell interactions, fostering the development of cardiac organoids with two distinct hollow chambers that contract in synchrony, mimicking arteriovenous rhythms.

($\Phi_{\text{PEG-COL}}$) of 4 and 10, we increased the porosity and hydrophilicity of the gel while reducing its elastic modulus.

We evaluated the extent to which gel properties influenced the ultrastructure and contractile function of cardiac organoids by modulating *E*-cadherin and *N*-cadherin expression. These features were assessed using various imaging techniques, including immunofluorescence staining, micro-computed tomography, and quantitative contraction analysis. We further evaluated the electrophysiological activities of the organoids by imaging intracellular calcium transients and using a wearable electromyography biosensor equipped with a microneedle array for real-time functional analysis [19]. To investigate the underlying mechanisms, we analyzed the expression of mesodermal, ectodermal, and *N*-cadherin genes. Overall, this study provides a strategy to overcome current limitations in building complex, multi-chambered cardiac organoids from diverse cell sources for disease modeling and regenerative medicine applications. The resulting organoid platforms will enable systematic investigation of how intrinsic genetic programs and extrinsic microenvironmental factors regulate cardiovascular tissue development, homeostasis, and diseases. Beyond cardiac applications, the underlying substrate design principles are readily extendable to the engineering of other tissue-mimicking organoids, supporting broader advances in *in vitro* human tissue models and translational research.

2. Results

2.1. PEG incorporation increases hydrophilicity and permeability of collagen gels while reducing their stiffness

Collagen-PEG gels with controlled permeability, hydrophilicity, and mechanical properties were prepared by neutralizing a mixture of acidic collagen stock solution and polyethylene glycol (PEG) with varied mass ratios of PEG to collagen ($\Phi_{\text{PEG-COL}}$) ranging from 0 to 4 and 10. We determined $\Phi_{\text{PEG-COL}}$ of 10 as the highest ratio, because the PEG-collagen solution with ratios above 10 did not fully form a gel (Fig. S2). Confocal images, captured using fluorescently labeled collagen molecules, showed that the collagen molecules self-associated into an interconnected fibrillar form regardless of $\Phi_{\text{PEG-COL}}$ (Fig. 1A). However, $\Phi_{\text{PEG-COL}}$ did affect the microstructure. Pure collagen gel with a $\Phi_{\text{PEG-COL}}$ of 0 exhibited a more compact and thinner fibrillar network than collagen-PEG gels with $\Phi_{\text{PEG-COL}}$ values of 4 and 10. Increasing $\Phi_{\text{PEG-COL}}$ from 4 to 10 resulted in a gel with a more loosely associated fibril network and a larger surface pore area (Fig. 1B). We also confirmed that the pore size increases with the increase in $\Phi_{\text{PEG-COL}}$ using scanning electron microscopy (SEM), and this result corresponds with the collagen fiber structure in the confocal images (Fig. S3).

Adding PEG to the collagen gel also increased its hydrophilicity. According to the Raman spectrum, the hydrogel surface presented the peak indicating the OH-stretching band (3280 – 3410 cm^{-1}), with the peak height being the highest at $\Phi_{\text{PEG-COL}}$ of 10 (Fig. 1C). Surface

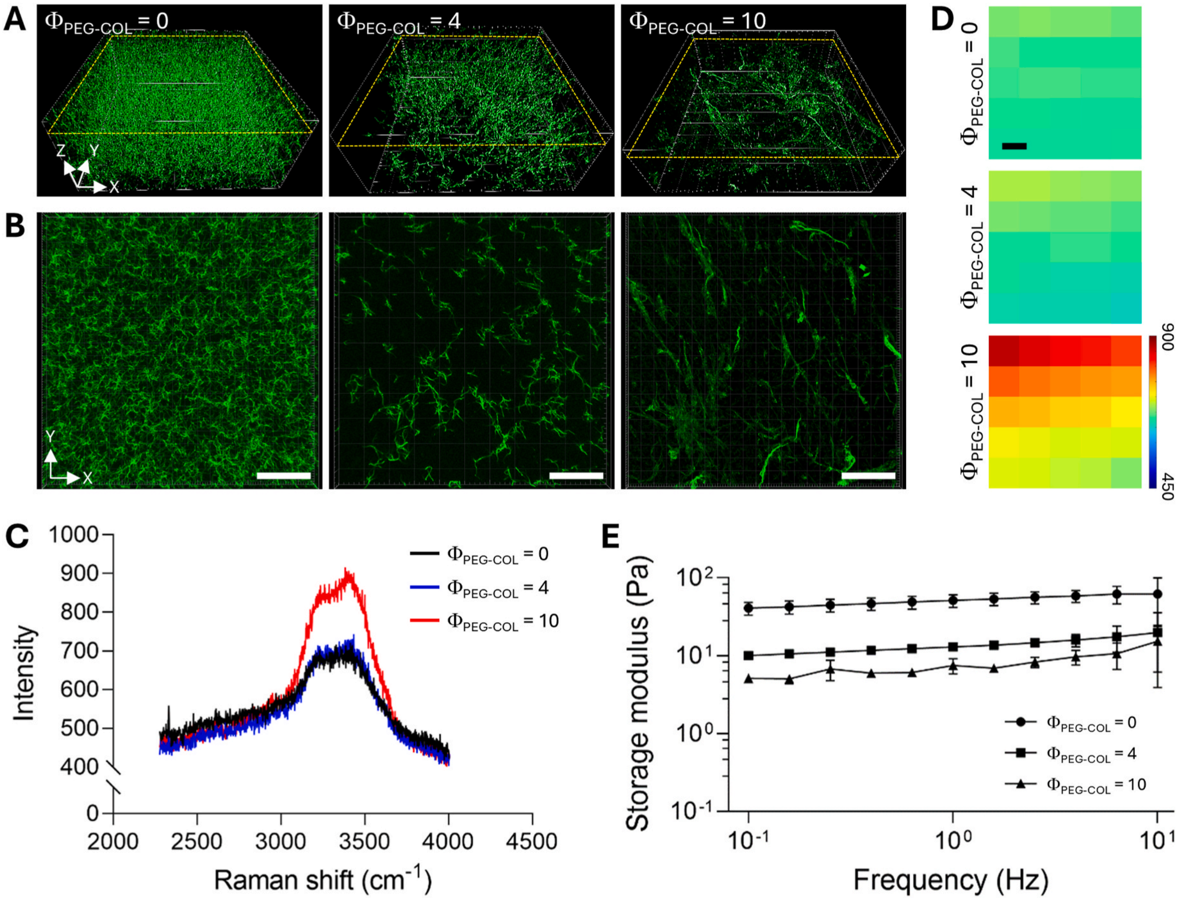

Fig. 1. Characterization of collagen-PEG hydrogels. (A) Confocal microscopy images of the 3D collagen fiber structure of the hydrogel reveal increased porosity with collagen-to-PEG mass ratios ($\Phi_{\text{PEG-COL}}$) of 0, 4, and 10 (Green: collagen). (B) 2D images of the collagen fiber organization also exhibit increased porosity with $\Phi_{\text{PEG-COL}}$ (Scale bar = 50 μm). (C) Confocal Raman spectra indicate a rise in water peak intensity with higher $\Phi_{\text{PEG-COL}}$ from 4 to 10. (D) Confocal Raman microscope mapping images show enhanced water retention in the gel with as $\Phi_{\text{PEG-COL}}$ increases (Scale bar = 1 μm). (E) The storage modulus of the hydrogels decreases with the increase in $\Phi_{\text{PEG-COL}}$ from 0 to 4, but no further decrease is observed between 4 and 10. (For interpretation of the references to color in this figure legend, the reader is referred to the Web version of this article.)

mapping of the Raman spectrum also revealed that increasing $\Phi_{\text{PEG-COL}}$ from 4 to 10 significantly increased the OH-stretching signal over the gel surface (Fig. 1D). We also confirmed that the water contact angle of the hydrogels decreases with increasing $\Phi_{\text{PEG-COL}}$ from 0 to 10, and that the released PEG concentration increases with increasing $\Phi_{\text{PEG-COL}}$ (Fig. S4A and Fig. S4B).

Furthermore, PEG incorporation into the collagen-PEG gel modulated its stiffness. A frequency sweep test, performed by oscillating gels within a linear viscoelastic region, showed that increasing $\Phi_{\text{PEG-COL}}$ from 0 to 4 and 10 decreased the storage modulus from ~30 to ~3 Pa. (Fig. 1E). The storage modulus was nearly independent of the frequency. We also estimated the degree of cross-linking from the measured elastic modulus, assuming the mechanics of the collagen-based gel can be described by rubber elasticity theory. The effective cross-linking density decreased with increasing $\Phi_{\text{PEG-COL}}$ from 0 to 10 (Fig. S4C). These results demonstrated that PEG incorporation disrupts collagen fiber connectivity, reducing effective network density. The equilibrium swelling ratio increases with increasing $\Phi_{\text{PEG-COL}}$ from 0 to 10 (Fig. S4D). This can be attributed to increased hydrophilicity introduced by PEG incorporation and a decrease in the effective crosslinking density of the collagen network. We measured the remaining mass and confirmed that there were no significant changes in all $\Phi_{\text{PEG-COL}}$ conditions (Fig. S4E).

2.2. PEG incorporation into collagen gels shifts EB behavior from surface migration to gel invasion

EBs prepared through suspension culture were placed on collagen-PEG gels with varied $\Phi_{\text{PEG-COL}}$. Within 7 days, EBs cultured on the pure collagen gel (i.e., $\Phi_{\text{PEG-COL}}$ of 0) began to dissociate, causing cells to migrate out (Fig. 2A to C). After 5 days of culture, the EB surface area increased by 19 ± 4 times due to active cell migration (Fig. 2D). Individual cells migrating out of the EB actively stretched actin filaments and elongated vinculin clusters on the cellular periphery, similar to cells spreading on a stiff substrate (Fig. 2E).

In contrast, EBs placed on the collagen-PEG hydrogels with $\Phi_{\text{PEG-COL}}$ values of 4 and 10 moved into the gel within five days, partially surrounded by interconnected collagen fibers of the gel (Fig. 2A and B). No dissociation or deformation of the EB was observed, unlike EBs placed on the pure collagen gel (Figs. 2C–3D). The immersion depth of EBs was greater with the higher $\Phi_{\text{PEG-COL}}$. Additionally, increasing the $\Phi_{\text{PEG-COL}}$ of the collagen-PEG gel from 4 to 10 decreased intracellular actin filament assembly as well as the expression and clustering of vinculin, a key marker of focal adhesions. (Fig. 2E).

2.3. Higher PEG content in collagen gels promotes cardiovascular differentiation, chamber formation, and coordinated contraction of EBs

EBs placed on the gel surface were incubated in the cardiomyocyte

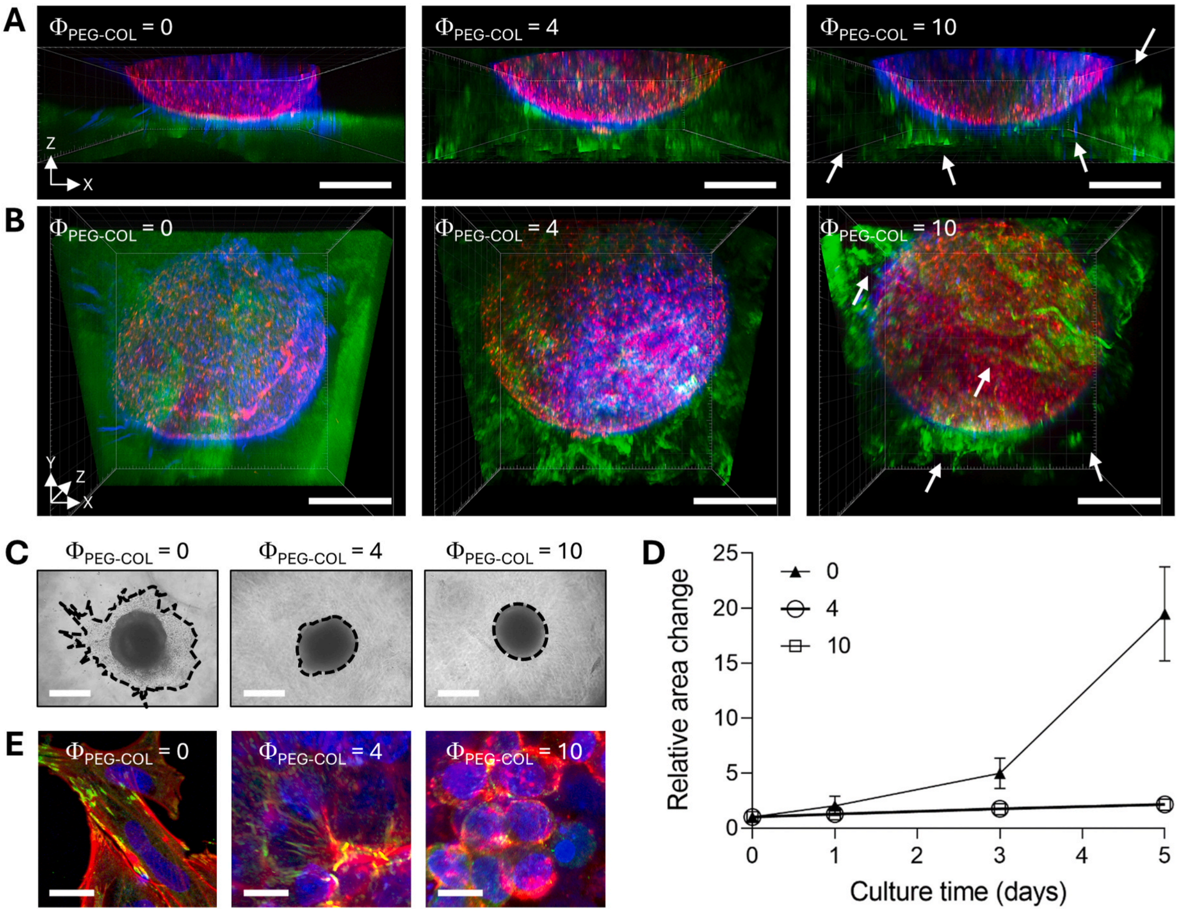

Fig. 2. Interaction between embryonic body (EB) and hydrogel. (A) 2D confocal images of EBs show that higher $\Phi_{\text{PEG-COL}}$ promotes more active EB invasion into the gel. (B) 3D confocal images show that EBs reorganizing loosely connected collagen fibers within the gel with $\Phi_{\text{PEG-COL}}$ of 10 during matrix invasion (Green: collagen, Red: F-actin, Blue: nucleus, Scale bar = 200 μm). (C) Phase contrast images of EBs after 7 days of culture on hydrogels with different $\Phi_{\text{PEG-COL}}$ of 0, 4, and 10 reveal active dissociation of EBs on the gel with $\Phi_{\text{PEG-COL}}$ of 0 (Scale bar = 500 μm). (D) Quantified relative area changes of EBs over 5 days show the most significant cellular dissociation on the gel with $\Phi_{\text{PEG-COL}}$ of 0. (E) Immunofluorescence images of the focal adhesion in cells from and within EBs highlight reduced actin fiber assembly, vinculin expression, and clustering at higher $\Phi_{\text{PEG-COL}}$ (Green: vinculin, Red: F-actin, Blue: nucleus, Scale bar = 10 μm). (For interpretation of the references to color in this figure legend, the reader is referred to the Web version of this article.)

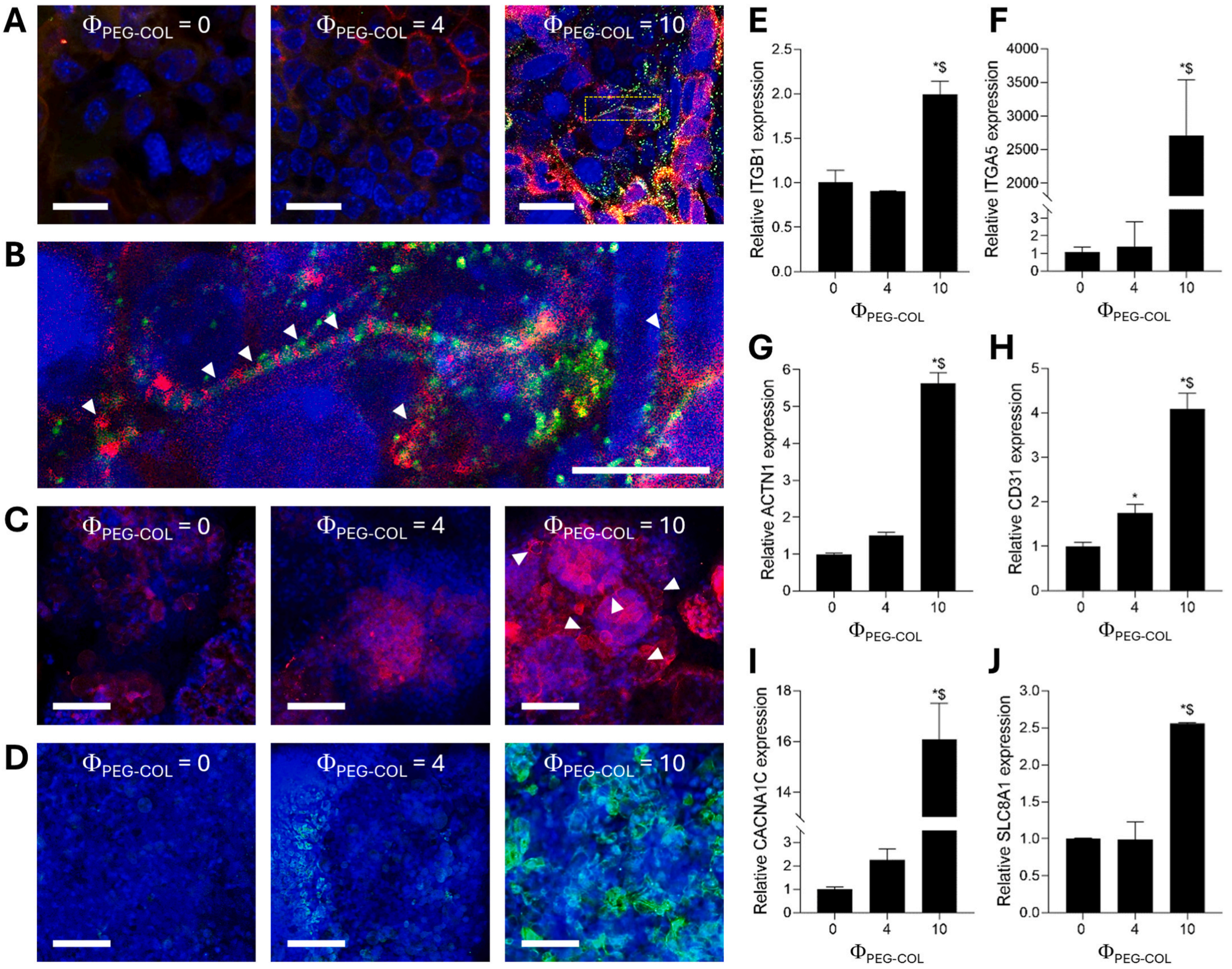

Fig. 3. Analysis of cardiovascular biomarkers in EBs cultured on gels with controlled $\Phi_{PEG-COL}$. (A) Immunofluorescence images of EBs differentiated on a gel with $\Phi_{PEG-COL}$ of 10 show enhanced expression of cTnT (green) and α-actinin (red). (Blue: nucleus, Scale bar = 20 μm). (B) Magnified view of sarcomeric actin structure from a section marked with the white box in (A) highlight Z-discs (white arrows) associated with α-actinin (Scale bar = 10 μm). (C) Immunofluorescence images of CD31-positive endothelial cells (red) indicate enhanced hollow lumen formation (white arrows) in EBs differentiated on the gel with $\Phi_{PEG-COL}$ of 10 (Blue: nucleus, Scale bar = 100 μm). (D) Immunofluorescence images of HCN4-positive pacemaker cells (green) show more abundant pacemaker cells within EBs differentiated on the gel with $\Phi_{PEG-COL}$ of 10 (Blue: nucleus, Scale bar = 100 μm). (E to J) Quantitative RT-PCR analysis of relative mRNA levels shows significantly higher expression of: (E) ITGB1, (F) ITGA5, (G) ACTN1, (H) CD31, (I) CACNA1C, and (J) SLC8A1 within EBs differentiated on the gel with $\Phi_{PEG-COL}$ of 10 after 14 days. * and $ indicate statistically significant differences ($p < 0.05$) between EBs differentiated on the gel with $\Phi_{PEG-COL}$ of 10 and those on gels with $\Phi_{PEG-COL}$ of 0 and 4, respectively. Values and error bars represent the average and standard deviation of ten samples per condition. (For interpretation of the references to color in this figure legend, the reader is referred to the Web version of this article.)

differentiation medium to activate the transition to cardiovascular organoids, as illustrated in Fig. S5. Over a 14-day culture period, EBs on the pure collagen gel and the collagen-PEG gel with a $\Phi_{PEG-COL}$ of 4 developed necrotic areas and teratoma-like structures, as shown in the histological cross-sections (Fig. S6). In contrast, EBs cultured on the collagen-PEG gel with $\Phi_{PEG-COL}$ of 10 formed structures resembling muscle bundles.

We further investigated the effect of the $\Phi_{PEG-COL}$ on the expression of cardiovascular biomarkers, including α-actinin and cardiac troponin T (cTnT). EBs on the pure collagen gel and the collagen-PEG gel with $\Phi_{PEG-COL}$ of 4 exhibited minimal expression of α-actinin and cTnT (Fig. 3A). In contrast, the collagen-PEG gel with $\Phi_{PEG-COL}$ of 10 led EBs to develop cardiac sarcomere actin structures, including Z-discs and cTnT (Fig. 3B). Additionally, these EBs exhibited an increased number of CD31-positive endothelial cells, with some forming hollow lumen-like structures (marked with white arrows in Fig. 3C). Notably, the gel with $\Phi_{PEG-COL}$ of 10 also promoted differentiation to HCN4-positive pacemaker cells compared to other conditions (Fig. 3D).

Quantitative RT-PCR analysis showed that EBs partially self-immersed in the collagen-PEG gel with $\Phi_{PEG-COL}$ of 10 exhibited a two-fold increase in integrin subunit β1 (ITGB1)-encoding mRNA and a 2710-fold increase in integrin subunit α5 (ITGA5)-encoding mRNA expression levels compared to those cultured on the pure collagen gel (Fig. 3E–F). The expression level of actin α1 (ACTN1)-encoding mRNA was 5.6 ± 0.3 times higher, and the CD31-encoding mRNA was also 4.0 ± 0.4 times higher than in EBs differentiated on the pure collagen gel. (Fig. 3G–H). Furthermore, the collagen-PEG gel with $\Phi_{PEG-COL}$ of 10 significantly increased the expression levels of calcium channel marker, calcium voltage-gated channel subunit alpha1 C (CACNA1C) and solute carrier family 8 member A1 (SLC8A1)-encoding mRNA, by 16 ± 1 and

2.6 ± 0.0 times, respectively, compared to the pure collagen gel (Fig. 3I–J).

Using micro-computational tomography (micro-CT), we investigated the 3D structure of EBs. EBs differentiated on the pure collagen gel exhibited a dome-shaped structure when cross-sectioned on the Z-axis computationally (Fig. 4A). In contrast, EBs differentiated in the collagen-PEG gel with $\Phi_{PEG\text{-}COL}$ of 4 maintained a 3D spherical shape (Fig. 4B). The 3D image cross-sectioned by the XZ- and XY-plane disclosed the formation of irregularly shaped multiple hollow space within the differentiated EBs.

When $\Phi_{PEG\text{-}COL}$ was increased to 10, the differentiated EBs presented an ellipsoidal structure (Fig. 4C). Interestingly, the differentiated EBs were divided into two distinct chambers. The larger, lower chamber had a conical shape with a blunt apex pointing downward, and the muscle layer surrounding this chamber was thicker on one side than the other, as shown in cross-sections along the XY-plane. In contrast, the upper chamber was surrounded by a thinner and more uniform muscle layer.

We segmented the hollow space to quantitatively analyze its morphology. In the 3D reconstructed images, the orange color represents the EB's body structure, while the green color indicates the hollow

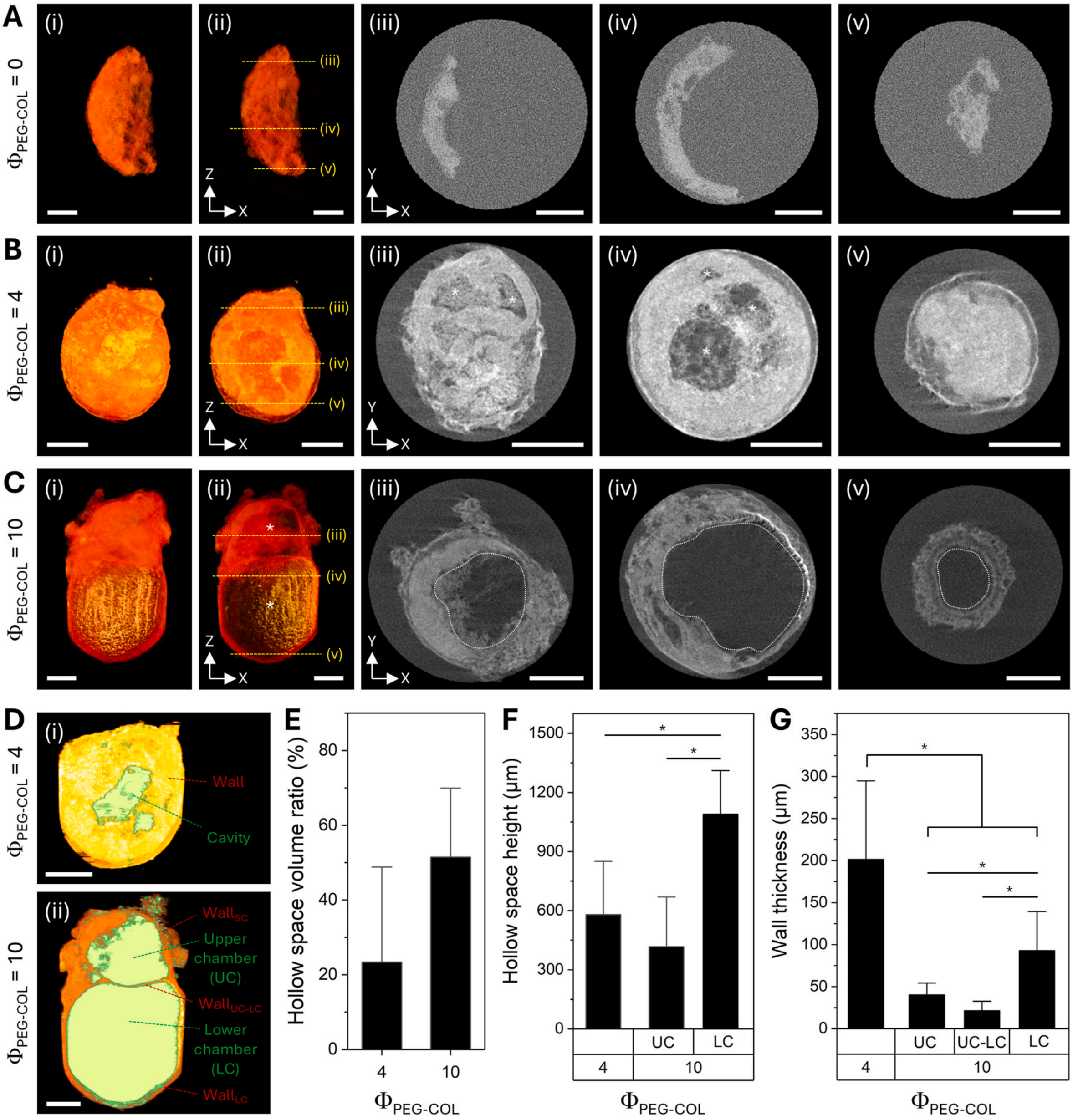

Fig. 4. Micro-CT images of EBs differentiated in collagen-PEG gels with varying $\Phi_{PEG\text{-}COL}$. EBs differentiated on (A) the pure collagen gel: (i) 3D image, (ii) 3D section view in XZ plane direction of a dome-shaped EB, (iii to v) Cross-sectional images in the XY-plane showing continuous cardiac muscle tissue, (B) the collagen-PEG gel with $\Phi_{PEG\text{-}COL}$ of 4: (i) 3D image, (ii) 3D section view in the XZ plane direction of a 3D spherical-shaped EB (iii to v) Cross-sectional images in the XY plane showing muscle tissue with multiple cavities (marked with *), (C) the collagen-PEG gel with $\Phi_{PEG\text{-}COL}$ of 10: (i) 3D image of an ellipsoidal-shaped EB, (ii) 3D section view in the XZ plane direction showing two hollow chambers (marked with *), (iii to v) Cross-sectional images in the XY plane showing muscle tissue surrounding two hollow chambers (white dotted line). Scale bars in (A to C) = 250 μm. (D) Segmentation images of EBs differentiated on collagen-PEG gels: (i) $\Phi_{PEG\text{-}COL}$ of 4 and (ii) $\Phi_{PEG\text{-}COL}$ of 10, illustrating differences in the inner hollow space morphology [Orange: muscle wall, Green: hollow spaces: cavity in (i) and upper and lower chambers in (ii), Scale bar = 250 μm]. (E) Volume ratio of hollow spaces. (F) Heights of hollow spaces ($^*p < 0.05$). In (E, F), values and error bars represent the average and standard deviation of four samples per condition. (G) Cardiac muscle thickness ($^*p < 0.05$). In (G), values and error bars represent the average and standard deviation of 15 measurements across three samples per condition. (For interpretation of the references to color in this figure legend, the reader is referred to the Web version of this article.)

space (Fig. 4D). Based on the segmented volumetric structure, we calculated the hollow space volume ratio (Fig. 4E). The EBs cultured on collagen-PEG gel with $\Phi_{\text{PEG-COL}}$ of 10 exhibited larger hollow space volume ratio than those with $\Phi_{\text{PEG-COL}}$ of 4. To compare space size, we identified two distinct chambers: the small upper chamber (UC) and the large lower chamber (LC) (Fig. 4F). We measured chamber height along the Z-axis. In the EBs on the collagen-PEG gel with $\Phi_{\text{PEG-COL}}$ of 10, the LC exhibited a significantly larger void volume than the UC and the cavity in the EBs on the gel with $\Phi_{\text{PEG-COL}}$ of 4. We also measured the wall thickness of the muscle layer between the inner and outer surface of the EBs (Fig. 4G). EBs cultured on the collagen-PEG gel with $\Phi_{\text{PEG-COL}}$ of 10 have three different muscle layers: (i) the wall around UC, (ii) the wall around LC, and (iii) the wall between UC and LC (UC-LC wall). In comparison, EBs on the collagen-PEG gel with $\Phi_{\text{PEG-COL}}$ of 4 had a significantly thicker muscle layer than any of the three walls in the EBs on the gel with $\Phi_{\text{PEG-COL}}$ of 10. Among the three layers in the EBs on the gel with $\Phi_{\text{PEG-COL}}$ of 10, the wall around the LC was the thickest, while the wall between the UC and LC was the thinnest.

More interestingly, EBs differentiated on the collagen-PEG gels with $\Phi_{\text{PEG-COL}}$ of 4 and 10 began contracting after ten days of differentiation, while those cultured on the pure collagen gel exhibited no contraction (Fig. 5A and Videos S1, S2, and S3). According to the quantitative analysis, EBs differentiated on the gels with $\Phi_{\text{PEG-COL}}$ of 10 contracted regularly every 0.8 s, while EBs differentiated on the gels with $\Phi_{\text{PEG-COL}}$ of 4 contracted irregularly. Also, collagen-PEG gels with $\Phi_{\text{PEG-COL}}$ of 10 increased the contraction area of differentiated EBs by seven times.

We further divided the EBs differentiated on the gels with $\Phi_{\text{PEG-COL}}$ of 10 into 18 different segments to evaluate whether the resulting organoids showed sequential contraction and relaxation, characteristic of atrioventricular synchrony (Figs. S7 and S8). We chose three segments

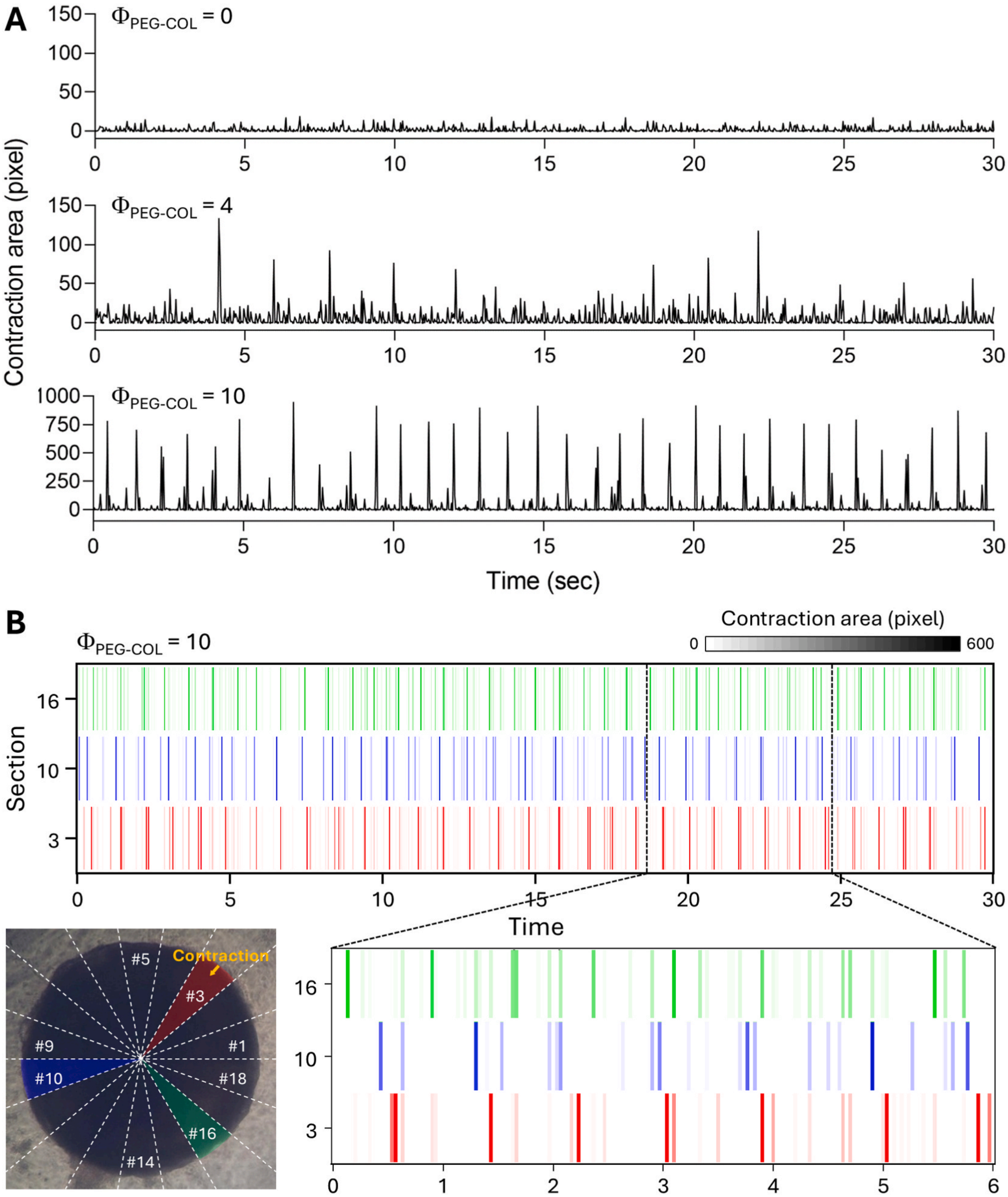

Fig. 5. Quantitative image analysis of the contraction behavior of differentiated EBs. (A) Measurement of the contraction area of EBs after 10 days of culture in cardiomyogenic differentiation media. EBs differentiated on the collagen-PEG gel with $\Phi_{\text{PEG-COL}}$ of 10 exhibit regular contractions, occurring every 0.8 s. (B) Repeated sequential contraction of segmented regions (#16, #10, and #3) in EBs differentiated on the collagen-PEG gel with $\Phi_{\text{PEG-COL}}$ of 10 over a 30-s period.

with more than 500 pixels change within 30 s, as marked with #3, #10, and #16, and analyzed their contraction sequence. As shown in Fig. 5B, the contraction initiated in section #16 prompted sequential contraction in section #10 and section #3. During the alternate localized contraction, the other areas remained relaxed. This sequential contraction was repeated regularly every 0.8 s.

2.4. Collagen-PEG gels enable heart-like electrophysiology in differentiated EBs

We evaluated the electrophysiological properties of EBs differentiated on collagen-PEG gels with varying $\Phi_{\text{PEG-COL}}$. First, we examined the intracellular calcium flux activity by measuring changes in fluorescence intensity over time using the Fluo-4 Direct Calcium Assay Kit, which produces fluorescence upon calcium-binding (Fig. 6A). As shown in both fluorescence images and quantitative image analysis (Fig. 6B), EBs differentiated on gels with $\Phi_{\text{PEG-COL}}$ of 0 and 4 showed limited intracellular calcium flux, as evidenced by minimal fluorescence change over time. In contrast, EBs differentiated on the gels with $\Phi_{\text{PEG-COL}}$ of 10 exhibited active calcium ion oscillation repeated every 0.8 s (Fig. 6B). The positive and negative changes in the fluorescence intensity ratio during oscillation were more than six times larger than those differentiated with gels having $\Phi_{\text{PEG-COL}}$ of 0 and 4.

Then, we determined the action potential of EBs differentiated on collagen-PEG gels. The flexible biosensor was placed on EBs differentiated to measure action potential (Fig. 6C). We confirmed that the biosensor contacted the EBs surface by using a fluorescence image. The action potential of differentiated EBs with 4 mV was detected every second for 4 s (Fig. 6D). We confirmed a single amplitude of differentiated EBs. The single amplitude had a P wave (depolarization of the atria) and QRS complex (depolarization of the ventricles) (Fig. 6D).

2.5. Matrix properties govern germ layer transcription and cadherin switching

We analyzed the expression of transcription factors related to embryo germ layers to examine how hydrogel properties regulate the cardiovascular differentiation of EBs. After three days of culture in the differentiation media, the expression levels of endoderm-specific GATA6 and α-fetoprotein (AFP)-encoding genes showed minimal dependence on $\Phi_{\text{PEG-COL}}$ (Fig. 7A–i). The mesodermal differentiation markers, goosecoid (GSC) and heart and neural crest derivatives expressed protein 1 (HAND1), as indicated by mRNA levels, were also independent of the $\Phi_{\text{PEG-COL}}$. In contrast, the SNAI1 gene expression increased with $\Phi_{\text{PEG-COL}}$ (Fig. 7A–ii). Moreover, EBs differentiated on collagen-PEG gels with $\Phi_{\text{PEG-COL}}$ of 4 and 10 exhibited a significant decrease in the ectoderm-specific gene, nestin (NES), but not tubulin β3 (TUBB3) (Fig. 7A–iii).

Further differentiation for 7 days altered the expression profiles of mesodermal and ectodermal-specific genes. The $\Phi_{\text{PEG-COL}}$ of the gel minimally influenced endoderm-specific GATA-6 and AFP gene expressions. (Fig. 7B–i). In contrast, GSC and HAND1 gene expression levels increased with $\Phi_{\text{PEG-COL}}$, whereas SNAI1 gene expression showed an inverse relationship with $\Phi_{\text{PEG-COL}}$ (Fig. 7B–ii). Similarly to

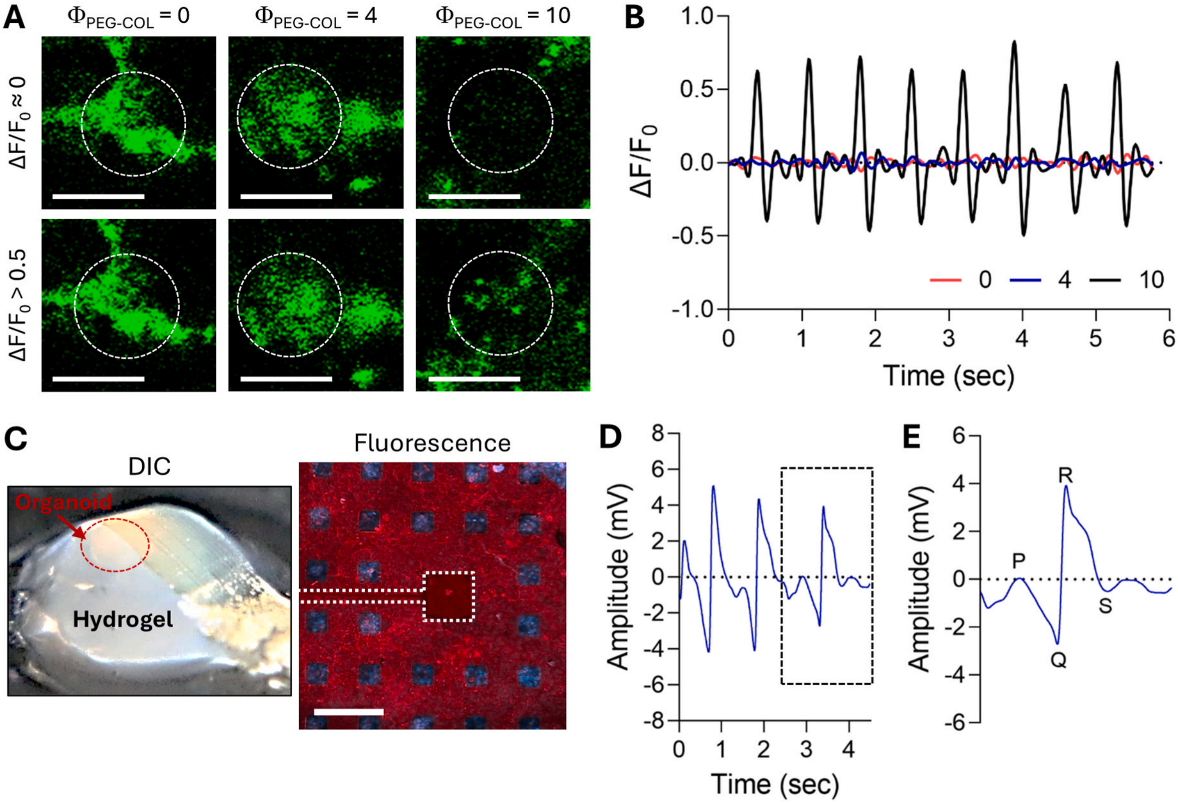

Fig. 6. Electrophysiological properties of EBs after 14 days of culture in the differentiation media. (A) Fluorescence imaging of intracellular calcium flux in EBs using the Fluo-4 assay kit. The first row shows images where the fluorescence intensity relative to the baseline ($\Delta F/F_0$) is close to 0. The second row shows that only EBs differentiated on the gel collagen-PEG gel with $\Phi_{\text{PEG-COL}}$ of 10 undergo positive changes in $\Delta F/F_0$ to 0.5. In contrast, EBs differentiated pm the pure collagen gel and the collagen-PEG gel with $\Phi_{\text{PEG-COL}}$ of 4 do not exhibit changes in $\Delta F/F_0$ (White circle: region of interest, Scale bar = 10 μm). (B) Quantified $\Delta F/F_0$ showed repeated positive and negative oscillations in EBs differentiated on the collagen-PEG gel with $\Phi_{\text{PEG-COL}}$ of 10. EBs cultured on the pure collagen gel and the collagen-PEG gel with $\Phi_{\text{PEG-COL}}$ of 4 exhibit minimal changes in $\Delta F/F_0$. (C) Differential interference contrast (DIC) and fluorescence images of EBs covered with a flexible biosensor to detect electrical signals after 14 days of differentiation (White dotted square: region where the biosensor is placed, Scale bar = 200 μm). (D) Electrocardiogram (ECG) amplitude plot from EBs differentiated on the collagen-PEG gel with $\Phi_{\text{PEG-COL}}$ of 10. (E) A single ECG signal was extracted from the black box in (D).

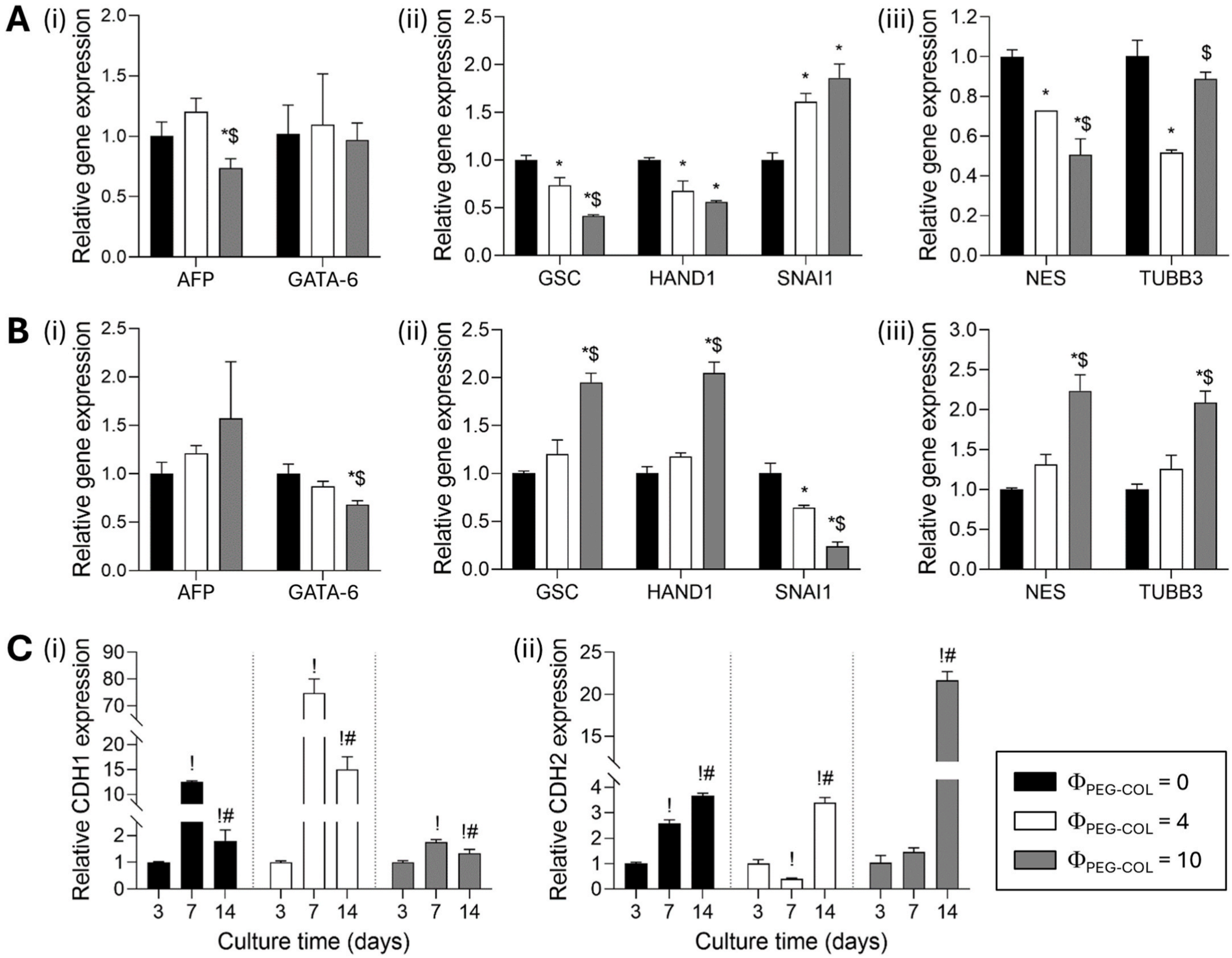

Fig. 7. Analysis of the expressions of transcription factors in EBs during differentiation. (A, B) Relative gene expression of germ layer-specific markers in EBs after (A) 3 days and (B) 7 days of culture in the differentiation media. In both (A) and (B), plots (i), (ii), and (iii) exhibit the endoderm, mesoderm, and ectoderm-specific mRNA levels, respectively. * and $ indicate the significant difference in values relative to EBs cultured on collagen-PEG gels with $\Phi_{PEG\text{-}COL}$ of 0 and 4, respectively. ($p < 0.05$). Values and error bars represent the average and standard deviation of ten samples per condition. (C) Relative gene expression of cadherin markers, (i) CDH1 and (ii) CDH2 in EBs cultured in differentiation media for 3, 7, and 14 days. ! and # indicate the significant difference in values relative to EBs cultured for 3 days and 7 days, respectively ($p < 0.05$). Values and error bars represent the average and standard deviation of ten samples per condition.

mesoderm-specific genes, expression levels of ectoderm-specific NES and TUBB3 genes increased with $\Phi_{PEG\text{-}COL}$ (Fig. 7B–iii).

In parallel, cadherin-encoding gene expression in EBs was monitored to examine effects of hydrogel properties on intercellular adhesion activities during differentiation. The expression of the cadherin 1 (CDH1)-encoding gene, responsible for *E*-cadherin synthesis, increased on Day 7 but decreased on Day 14 in all groups. The magnitude of these changes was most minor in EBs differentiated in the collagen-PEG gel with $\Phi_{PEG\text{-}COL}$ of 10 (Fig. 7C–i). In contrast, the expression of cadherin 2 (CDH2)-encoding gene, responsible for *N*-cadherin synthesis, increased over time in all groups. Interestingly, the dependency of CDH2 levels on time was most significant in EBs invading the collagen-PEG gel with $\Phi_{PEG\text{-}COL}$ of 10 (Fig. 7C–ii).

3. Discussion

Collagen, a major ECM component, plays a significant role in embryonic tissue and organ development [17,20]. It not only has a cell adherent GFOGER domain but also cross-links and/or entangles to form fibrillar networks that generate an elastic response [17]. Adding PEG to a pre-gelled collagen solution resulted in collagen fiber networks with increased spacing, as shown by immunofluorescence imaging (Fig. 1A–B). This is likely because PEG reduces the association of water molecules with collagen via hydrogen bonds, affecting the formation of the triple helical structure of collagen gel [18,21]. Consequently, increasing $\Phi_{PEG\text{-}COL}$ made the collagen gel more hydrophilic, as illustrated with Raman spectroscopy (Fig. 1C–D). PEG also made the gel softer, as verified by the storage modulus representing stiffness. However, similar independence of the storage modulus on frequency with the low-amplitude oscillatory shear measurement indicates that the gel behaves elastically across $\Phi_{PEG\text{-}COL}$. Overall, PEG incorporation enabled tuning of ECM properties while maintaining a constant integrin-binding ligand density.

One notable finding is that collagen-PEG gels with greater permeability and hydrophilicity, coupled with reduced stiffness, significantly facilitated EV invasion into the matrix. Specifically, the collagen in the gel was essential to immobilize EBs placed on the gel because the pure PEG gel does not allow cellular attachment. Then, the collagen-PEG hydrogel with $\Phi_{PEG\text{-}COL}$ of 10 enabled gravity-induced invasion of EBs, similar to the embryo implantation process [13]. In contrast, EBs placed on the pure collagen gel, which was stiffer and less permeable than the collagen-PEG gel, promoted focal adhesion formation and cell migration on the gel matrix due to cellular mechanosensing ability [22,23]. Therefore, we suggest that the collagen-PEG gel reduces adhesion of cells in EBs to the collagen gel in proportion to $\Phi_{\text{PEG-COL}}$, as illustrated with reduced focal adhesion (Fig. 2). This reduced cell-matrix interaction likely led cells to retain their intercellular adhesion within EBs, as confirmed by the increased expression of the *N*-cadherin-encoding gene over time (Fig. 7C). It is possible that EBs on the collagen-PEG gel reduced mechanosensitive RhoA/ROCK signaling, leading to decreased cellular contractility. This reduction in contractility could limit individual cell migration outward, promoting the collective reorganization of cells within EBs. Taken together, these results demonstrate that the invasion and aggregation of embryoid bodies into heart-like organoids can be facilitated by engineering the hydrogel's biophysical properties to mimic the dynamic microenvironment of the embryonic heart development process. Information on the stiffness of the mouse endometrium is lacking, and reported values for the human endometrium range from tens to thousands of pascals, depending on the secretory phase and the measurement technique used [24,25]. Therefore, although it is challenging to directly compare our results with the physiological stiffness range of the target tissue, the stiffness of the collagen-PEG gel used in this study is not only close to the reported physiological range but also has porosity and hydrophilicity, facilitating the formation of embryo-like cardiac organoids.

Another important finding is that the collagen-PEG gel with $\Phi_{\text{PEG-COL}}$ of 10 facilitated the differentiation of EBs to several cell populations found in a native heart. The heart consists of morphologically and functionally distinct chambers [26]. Cardiac muscle surrounds individual chambers to perform synchronized contraction and relaxation in response to electric signals from a sinus node [26]. The differentiated EBs consisted of cardiomyocytes, identified by positive staining of sarcomeric α-actinin and cardiac troponin T (Fig. 3B–C). Moreover, these differentiated EBs exhibited sarcomere Z-lines, which are structures enabling cardiomyocyte contraction, thereby confirming myocardium formation [27,28]. These EBs also displayed clusters of pacemaker cells, which are located in a sinoatrial node of the heart and generate rhythmic electrical impulses, as well as endothelial cells that form blood vessel-like hollow lumens (Fig. 3D) [29,30]. In contrast, the pure collagen gel minimized cardiovascular differentiation of EBs, illustrating the important role of the extracellular microenvironment. In the present study, we were unable to perform flow cytometry or single-cell RNA sequencing due to technical challenges in dissociating intact organoids into viable single-cell suspensions. Quantitative cell profiling, which will provide a more precise assessment of relative cardiac cell populations within organoids, will be an important direction for future studies.

The difference in the cardiovascular differentiation between conditions was reflected in their gene expression levels (Fig. 3). Specifically, the collagen-PEG gel with $\Phi_{\text{PEG-COL}}$ of 10 showed increased expression levels of CACNA1 and SLC8A1 genes. CACNA1 genes encode the voltage-gated calcium channel L-type subunit, which induces cardiac calcium influx, while SLC8A1 is involved in the sodium ion-calcium ion exchanger [31,32]. These results indicate that gel substrates enabling EB invasion promoted cardiomyocytes with essential calcium handling proteins.

More interestingly, the collagen-PEG hydrogel with $\Phi_{\text{PEG-COL}}$ of 10 led to the formation of a two distinct-chambered structure, similar to an embryonic heart consisting of a single sinus venosus and a single ventricle (Fig. 4C) [33]. We interpret that the balanced cell-matrix and cell-cell interaction within EBs due to invasion into the gel matrix was essential for the formation of two hollow chambers. Likely due to electrical impulses from pacemaker cells, EBs with these two distinct chambers spontaneously repeated sequential contraction with a regular tone, similar to atrioventricular synchrony (Fig. 5). Similarly, calcium influx, which is responsible for the contraction of cardiomyocytes, was most active within the two-chambered organoids (Fig. 6A–B). The frequency of the change in fluorescence signal caused by intracellular calcium concentration change was similar to the electrocardiogram (ECG) signal collected with an electrochemical biosensor installed on the two-chambered organoid (Fig. 6C–E). The frequency of the change in fluorescence signal caused by intracellular calcium concentration change was similar to the electrocardiogram (ECG) signal collected with an electrochemical biosensor installed on the two-chambered organoid (Fig. 6C–E). Compared with previous studies measuring heart rate *in vivo* in mouse embryos, our study demonstrated that the robust contraction activity of the heart organoid is consistent with early-stage activity in mouse heart development [34,35]. In a previous study, the QRS complexes of the human heart organoid appeared approximately 0.3 s, which is slower than the reported QRS duration of the human embryonic heart [36]. Similarly, the organoid in this study exhibited QRS complexes of approximately 0.5 s, slower than those of the mouse embryonic heart, but it demonstrated well-defined electrophysiological activity patterns consistent with the *in vivo* sinus rhythm. These results confirm that pacemaker cells and cardiomyocytes in the two-chambered organoid are functional in reproducing electrophysiological characteristics of the *in vivo* embryonic heart. These results confirm that pacemaker cells and cardiomyocytes in the two-chambered organoid are functional in reproducing electrophysiological characteristics of the *in vivo* embryonic heart. Furthermore, it is likely that asymmetric cardiac muscle layer thickness between the top sinus venous-like chambers and the bottom ventricle-like chambers, as shown with micro-CT images (Fig. 4), contribute to reproducing the atrioventricular synchrony-like contraction activity.

Furthermore, this study revealed that the effects of gel substrate properties on cardiovascular organoid formation could be explained by the temporal expression patterns of the mesoderm and ectoderm layer-specific genes. First, SNAI1, GSC, and HAND1 genes are known to be important factors in mesoderm development [37–39]. SNAI1 is an essential factor for the epicardial epithelial-mesenchymal transition (EMT). Both GSC and HAND1 genes promote the proliferation, differentiation, and positioning of cardiac progenitor cells, thus influencing cardiac morphogenesis. Specifically, the HAND1 gene is crucial for the development of the ventricle. With the mesoderm-specific gene expression patterns shown in Fig. 7A–(ii) and 7 B-(ii), we propose that the collagen-PEG gel with $\Phi_{\text{PEG-COL}}$ of 10 stimulates the expression of the SNAI1 gene earlier than other substrates. The early increase in the SNAI1 gene is also well related to the limited increase in the *E*-cadherin-encoding CDH1 gene but a significant increase in the *N*-cadherin-encoding CDH2 gene. As *N*-cadherin acts as the main adherence junctions of cardiogenesis, these results confirm that the collagen-PEG gel with $\Phi_{\text{PEG-COL}}$ of 10 promotes the EMT within EBs more significantly than the other two conditions (Fig. 7C) [37].

This increased SNAI1 gene expression, which represses the expression of the *E*-cadherin gene, likely stimulated increases in the expression of GSC and HAND1 genes that play significant roles in tissue morphogenesis, thus forming a two-chambered organoid. There is no evidence that SNAI1 regulates GSC and HAND1 gene expressions directly. However, it is found that expression levels of the GSC and HAND1 genes increase during the epithelial-mesenchymal transition [40]. Additionally, EBs differentiated on the collagen-PEG gel with $\Phi_{\text{PEG-COL}}$ of 10 showed the higher expression of ectoderm-specific genes, including NES and TUBB3 genes, particularly on Day 7. Both NES and TUBB3 are markers of neuronal development, thus implying the development of autonomous neurons that can control the beating rate of differentiated EBs. Such neural innervation effect will be studied systematically in future studies [41–43].

We propose that the *in situ* bottom-up approach to cardiovascular organoid assembly—achieved through the differentiation of EBs within a proper microenvironment—should be recognized as distinct from conventional top-down methodologies. In the latter, pre-differentiated cells are co-cultured and organized into organoids using sophisticated biofabrication tools. By contrast, our method harnesses the intrinsic self-organization capacity of EBs in a minimally engineered yet precisely tuned system. An important feature of this approach is the transparency of the gel substrates, which facilitates real-time bioimaging to monitor intracellular processes such as calcium flux, as demonstrated in Fig. 6A. Additionally, as shown in Fig. 6B, this organoid platform can be integrated with wearable biosensors to track electrophysiological activities. This capability will enable dynamic monitoring under both normal and pathological conditions, making it a powerful tool for studying cardiovascular function and disease.

We envision that this straightforward assembly method will significantly contribute to cardiovascular research. This reliable platform will enable the systematic evaluation of environmental toxins, immunogens, and novel drug candidates for their potential impacts on human cardiovascular systems. Furthermore, the simplicity of the experimental setup allows it to be easily adapted to a variety of microphysiological systems, designed to model specific perturbations such as injury or disease. This adaptability facilitates precise assessments of the therapeutic efficacy of drug molecules, regenerative cells, and their derivatives, including exosomes. Our findings can also be extended to the development of human cardiovascular organoids. For example, induced pluripotent stem cells (iPSCs) derived from human tissues could similarly respond to the physical and biochemical properties of the gel substrate, potentially forming organoids with enhanced complexity. Such organoids may exhibit chambered structures and physiological functions, such as synchronized arteriovenous contractions, further advancing their resemblance to human heart tissue.

This study demonstrates that the microstructure and physical properties of collagen gels, where EBs undergo differentiation, play a critical role in regulating cell-cell interaction and, subsequently, differentiation, as well as the morphology and physiological function of the resulting cardiovascular organoids. Notably, the collagen-PEG gel with $\Phi_{\text{PEG-COL}}$ of 10, characterized by greater permeability and hydrophilicity and reduced stiffness compared to a pure collagen gel, enabled EB invasion into the gel matrix. These EBs were developed into organoids featuring two distinct hollow muscle chambers, associated with pacemaker and endothelial cells. These organoids exhibited key functional attributes, including sequential arteriovenous synchrony-like contractions of the two chambers and repeated calcium flux. In contrast, EBs differentiated on pure collagen gels showed limited contraction and calcium transients. Furthermore, integrating a wearable biosensor with the organoid successfully detected a P wave and QRS complex, demonstrating its potential for electrophysiological monitoring. The observed effects of gel properties on organoid quality were linked to increased expression of genes indicative of mesodermal and ectodermal differentiation, as well as genes encoding *N*-cadherin. Overall, these findings underscore the significance of finely tuning the substrate environment to enhance organoid development and function.

4. Materials and methods

4.1. Fabrication and characterization of collagen-polyethylene glycol (PEG) hydrogel

Collagen-polyethylene glycol (PEG) hydrogels were prepared as previously described [17]. In brief, hydrogels were formed through *in situ* cross-linking of collagen molecules by mixing PEG (MW 7500, Polysciences) with bovine type I collagen (3 mg/mL, Advanced Biomatrix) in an equal volume of serum-free ESC medium. The mass ratios of PEG to collagen were changed from 0 to 4 and 10. Reconstitution solution (0.26 M sodium hydrogen carbonate, 0.2 M HEPES, and 0.04 M sodium hydroxide) was added to initiate gel formation. Then, the pre-hydrogel solution was incubated at 37 °C for at least 30 min.

The fibrillar collagen structure of the gel was examined by imaging the fluorescently labeled collagen. The fluorescent labeling of collagen was performed as previously described [44]. Briefly, the collagen gels were formed in a 100 mm-diameter culture dish. Borate buffer (50 mM boric acid, pH 9.0) was added to the gel and incubated for 15 min at room temperature (RT). The dye solution (1.132 μg/mL Atto-488 NHS-ester dye in borate buffer) was added to the gel for 1 h at RT. Then, Tris buffer (50 mM Tris, pH 7.4) was added to the gel for 10 min to quench the dye reaction. The gel was liquefied into the collagen solution using 500 mM acetic acid. The resulting fluorescent collagen was mixed with unlabeled collagen at a volume ratio of 1:4 to prepare collagen-PEG hydrogels with different PEG-to-collagen mass ratios ($\Phi_{\text{PEG-COL}}$). The resulting gels were imaged using a laser scanning confocal microscope (LSM 710, Zeiss).

For SEM analysis, collagen-PEG gels were prepared by freeze-drying to preserve their internal microstructure. The dried samples were subsequently sputter-coated with platinum to a thickness of approximately 50 nm. The microstructures of the gels were then observed using a scanning electron microscope (FEI Quanta FEG 450, FEI Company).

The water content on the gel surface was evaluated using a Raman confocal microscope (LabRAM HR 3D, Horiba). The hydrogel installed in the well-chamber plate was examined with a laser excitation source. Then, the water distribution in the gel was mapped using MATLAB (MathWorks) based on the acquired data.

The properties of the hydrogel were characterized using a rheometer (DHR-2, TA Instruments). The hydrogels were placed between two plates (Diameter = 22 mm) with a 200 μm gap. Oscillation at 0.1% strain was applied to the gel, with frequencies ranging from 0.1 to 4 Hz. The resulting stress of the gel was used to quantify storage modulus and loss modulus at each frequency.

Hydrophilicity of the Collagen-PEG gels were evaluated by water contact angle measurements. Hydrogels were prepared with a parallel flat surface, and a droplet of deionized water was gently placed onto the surface. After stabilization of the droplet, the contact angle was measured using a contact angle goniometer (Ramé-Hart Model 250 Contact Angle Goniometer).

Total PEG content in released samples was quantified using the barium-iodide colorimetric assay as previously described [45]. Collagen-PEG gels were fabricated and washed according to their respective preparation protocols. The samples were then incubated in molecular-grade water for 5 days, after which the supernatants were collected. The collected supernatants were used to quantify the amount of PEG released from the hydrogels. For measurement, aliquots of each sample or standard were mixed with $BaCl_2$ solution followed by the iodine/iodide solution, and the mixture was incubated at room temperature for color development. The absorbance was measured at 535 nm on a microplate reader, and PEG concentrations were determined from the standard curve.

The effective crosslink density of each collagen gel was estimated using rubber elasticity theory assuming an affined network model, according to equation (1), where S is the shear modulus obtained from mechanical testing and Q is the degree of swelling [46]. Given the fibrous and physically crosslinked nature of collagen networks, the calculated ν_e presents an effective load-bearing network connectivity parameter rather than an absolute chemical crosslink density.

$$\nu_e = \frac{SQ^{\frac{1}{3}}}{RT} \tag{1}$$

To evaluate the swelling behavior of the collagen-PEG gels, freeze-dried gels were allowed to equilibrate in PBS at room temperature until swelling equilibrium was reached. The equilibrium swelling ratio was calculated based on the mass of the gel in the dried state prior to swelling and the mass in the swollen state, after gently removing excess surface water.

For degradation analysis, collagen-PEG gels were incubated in PBS at 37 °C. On day 7 after incubation, the samples were collected, thoroughly washed, and freeze-dried to determine dry mass. The degree of degradation was quantified by measuring the remaining dry mass and normalizing it to the initial mass of each hydrogel.

4.2. Assembly and characterization of embryonic bodies (EBs) using embryonic stem cells (ESCs)

Mouse ESCs (AB2.2, ATCC) were cultured on plates coated with 0.1% gelatin in high glucose Dulbecco's Modified Eagle Medium (Corning) supplemented with [15% ESC-certified fetal bovine serum (FBS), 0.1 mM 2-mecaptoethanol, 1X MEM nonessential amino acid, 1000 U/mL mouse leukemia inhibitory factor, and 1% penicillin-streptomycin (PS)]. Mouse ESCs with a passage number below fifteen were used for all experiments. All ESCs were cultured under standard culture conditions (37 °C, 5% CO_2, 95% humidity).

To prepare EBs, mouse ESCs were detached using TrypLE Express (Gibco). EBs were formed using hanging drop culture. Briefly, cells suspended in phosphate buffer saline (PBS) were pipetted onto the lids of culture dishes, which were then inverted over a dish containing 10 mL of PBS to maintain humidity. Individual EBs were formed with 2000 mouse ESCs within 3 days.

EBs were placed on collagen and collagen-PEG hydrogels and cultured in general ESC growth media. Morphological changes of EBs were monitored using a phase-contrast microscope (CK2, Olympus). The images were used to quantify the surface area of EBs for 5 days using ImageJ. The relative area change of EBs was calculated with the ratio between the surface area of EBs on Days 0, 1, 3, and 5 days and that of EBs before transfer to the gel.

Immunofluorescence staining of EBs was performed to analyze focal adhesion formation. After 5 or 7 days of cultures on the gel surface, EBs were fixed in 4% paraformaldehyde solution at RT for 15 min. EBs were then permeabilized with 0.1% Triton X-100 solution for 10 min and blocked with a buffer containing 5% FBS and 0.1% Tween-20 for 1 h. EBs were incubated overnight at 4 °C with primary antibodies against vinculin (1:100 dilution in blocking buffer). Subsequently, EBs were incubated with secondary antibodies (anti-mouse conjugated Alexa 488, 1:100 dilution) and phalloidin-Alexa 555 (1:100 dilution) for 1 h at RT. 4′,6-Diamido-2-phenylindole (DAPI) was used to stain cell nuclei (1:1000 dilution). Images were captured using a confocal microscope (LSM 700, Zeiss). 3D images were reconstructed using Imaris (Oxford Instruments).

4.3. Analysis of EB differentiation to a cardiovascular organoid

Mouse EBs, prepared through the hanging drop culture, were placed on collagen and collagen-PEG hydrogels immersed in a growth medium. The PSC cardiomyocyte differentiation kit (Gibco) was used to induce differentiation of the EBs into cardiovascular organoids. The differentiated EBs were harvested and lysed on Days 3, 7, and 14 for subsequent analysis.

Immunofluorescence staining was performed with organoids on Day 14. The differentiated EBs underwent sequential fixation, permeabilization, and blocking as described in the previous section for EBs. They were then incubated with primary antibodies to cTnT, α-actinin, CD31, or HCN4 at 4 °C overnight. The antibodies were diluted in a blocking buffer at a 1:100 ratio. Afterward, the EBs were incubated with secondary antibodies, either anti-mouse conjugated Alexa 488 or 555 (1:100 dilution) and anti-rabbit conjugated Alexa 488 (1:100 dilution), for 1 h at RT. DAPI (1:1000 dilution) was used to stain the nuclei. Images were captured using a confocal microscope (LSM 700, Zeiss).

Gene expression levels in the differentiated EBs were assessed via real-time (RT) PCR. Genes encoding cardiomyogenic markers and calcium handling markers were analyzed after 14 days of differentiation. Germ layer development and cadherin expression during differentiation were also examined using RT-PCR. EBs were collected from the gels on Days 3, 7, and 14 by incubating them in an organoid harvest solution at 4 °C for 1 h mRNA was purified using a RNeasy Mini Kit (Qiagen) and quantified using a Nanodrop spectrophotometer (Thermo Scientific).

Next, cDNA was synthesized using a thermal cycler (MyCycler™, Bio-Rad) by mixing 1 mg of mRNA with the iScript cDNA synthesis kit in a 20 μL reaction volume according to the manufacturer's instructions. The synthesized cDNA was used in RT-PCR reactions performed with SYBR Premix (iTaq Universal SYBR® Green Supermix, Bio-Rad). The reactions, consisting of 40 cycles, were carried out in an RT-PCR machine (Lightcycler® 480, Roche). Each cycle included melting at 95 °C for 15 s, followed by annealing and extension at 60 °C for 60 s for each primer pair.

Real-time PCR data were analyzed using the comparative threshold cycle (Ct) method. Relative expression of each gene compared to the expression level of GAPDH was determined and normalized to the expression level of differentiated EBs cultured on the collagen hydrogel or 3-day cultured organoid. Each gene amplification assay was performed in triplicate. Melting curves were performed, and negative controls were included to verify the absence of primer dimers. The analyzed genes and their corresponding specific primers are listed in Table S1.

4.4. Analysis of the 3D structure of differentiated EBs

The 3D structure of differentiated EBs was observed using Bio micro-CT (MicroXCT-400, Xradia). EBs cultured in the cardiomyogenic differentiation media for 14 days were fixed with 4% paraformaldehyde solution overnight at 4 °C. Then, EBs were immersed in the Lugol solution (Iodine/Potassium iodide solution) for at least 72 h. The Lugol solution was removed immediately before micro-CT measurement. The EBs were washed once with DI water. The EBs were then scanned with micro-CT while immersed in DI water. The micro-CT scan parameters were as follows: 8 W of power, 45 kV of voltage, and 176 μA of electric current. All micro-CT images were processed using Xradia image software (Zeiss).

2D planar images were extracted from the 3D volumetric data acquired. These planar images were processed using MATLAB to quantify the hollow space through three steps: (i) image denoising, (ii) object segmentation of the organoid body, and (iii) segmentation of hollow space from the organoid body. Based on the segmented area from each 2D planar image, the 3D volumetric structure of the organoid body and hollow space was reconstructed. Finally, the volume ratio between the organoid body and the hollow space, hollow space height, and wall thickness of muscle layer were calculated.

4.5. Image analysis of contraction mode of differentiated EBs

The contraction of the differentiated EB was observed using a phase contrast microscope (CK2, Olympus) after ten days of differentiation. We extracted 900 images from 30 s of video (30 frames/s) that recorded the EBs' beating under the optical microscope. The sequence of contraction image processing using MATLAB consists of three steps: (i) object segmentation of EBs, (ii) subtraction between frames to acquire contracted area, and (iii) radial division into 18 sections. The sections were divided at 20-degree intervals based on the central mass of the heart organoid, and values of the expanded area were excluded from the results. Finally, the contracted area was calculated by counting the number of pixels within each section.

4.6. Calcium flux imaging of differentiated EBs

The EBs differentiated for 14 days were incubated in a medium containing the calcium indicator from Fluo-4 Direct Calcium Assay Kit (Invitrogen) for 1 h. Imaging was performed at RT using the time series mode of a laser scanning confocal microscope (LSM 710, Zeiss). We acquired 100 images with 30 frames per second to analyze calcium fluxes. First, all images corresponding to the ROI where the signal blinking occurred were cropped using MATLAB. The signal intensity of pixels in the green channel of the cropped images was then averaged.

Calcium transient amplitude ($\Delta F/F_0$) was calculated as the difference between peak and baseline calcium fluorescence (ΔF) divided by the baseline fluorescence level (F_0).

4.7. ECG analysis of contraction of differentiated EBs

The flexible biosensor with a gold electrode was fabricated as previously described [47]. The process began by spin-casting layers of polymethyl methacrylate (PMMA) and polyimide (PI) on a Si substrate. The thickness of each layer was 1 μm. Next, thin films of Ti/Au (5 nm/150 nm) were deposited using an electron-beam (e-beam) evaporator. The thin metallic film electrodes and interconnecting traces were defined by photolithography with a photoresist (AZ 1518, 3000 rpm, 30 s) and subsequent wet etching in solutions of Ti and Au etchants (Transene, Inc.). An encapsulation layer of PI (1 μm thick) was then spin-casted on top and patterned by photolithography with a photoresist (AZ 9260, 3000 rpm, 1 min) and oxygen plasma reactive ion etching to define the electrode openings. To measure the electrocardiogram (ECG) signals of the cardiac organoid, flexible ACF cables were used to connect the system to the flexible sensor sheet, which was placed on the organoid surface to make conformal contact. The ECG signals were acquired and amplified by a PowerLab and Bio Amps system (AD Instruments) and post-processed using LabChart after being sampled at 10 kHz and low pass filtered at 3 kHz (AD Instruments).

4.8. Statistical analysis

Quantitative values are expressed as means ± standard deviations. GraphPad Prism 9 software (La Jolla) was used to perform a one-way analysis of variance (ANOVA) with Tukey's honest significant difference (HSD) test and Student's t-test for pair-wise comparison. *P*-values less than 0.05 were considered to indicate statistically significant differences.

CRediT authorship contribution statement

Eun Mi Kim: Writing – original draft, Visualization, Validation, Methodology, Formal analysis, Data curation, Conceptualization. **Yujin Ahn:** Writing – review & editing, Visualization, Validation, Software, Formal analysis, Data curation. **Jason Wang:** Investigation, Data curation. **Joanne Hwang:** Investigation, Data curation. **Junggeon Park:** Investigation, Data curation. **Kai-Yu Huang:** Data curation. **Seulgi Kim:** Data curation. **Sujeong Kim:** Data curation. **Roy D. Dar:** Methodology, Investigation. **Young Jun Kim:** Methodology. **Heungsoo Shin:** Writing – review & editing, Supervision, Funding acquisition. **Chi Hwan Lee:** Writing – review & editing, Supervision, Funding acquisition. **Hyunjoon Kong:** Writing – review & editing, Writing – original draft, Supervision, Project administration, Funding acquisition, Conceptualization.

Funding

H. Kong acknowledges funding support from the National Science Foundation (CBET-2032521, CBET-2229523, Expeditions-2123781), the National Institute of Health (R61/R33 HL159948), and a Chan Zuckerberg Biohub Chicago Research Award. C. H. Lee acknowledges funding support from the National Science Foundation (CBET-2032529). H. Shin acknowledges funding support from the National Research Foundation of Korea funded by the Korean government (RS-2023-00207983). Y. Ahn acknowledges funding support from a Chan Zuckerberg Biohub Chicago Acceleration Postdoctoral Program and the Korea Health Technology R&D Project through the Korea Health Industry Development Institute funded by the Ministry of Health and Welfare (HI19C1095). Y. J. Kim acknowledges funding support from the Ministry of Food and Drug Safety of the Republic of Korea (RS-2024-00331852).

Declaration of competing interest

The authors declare that they have no known competing financial interests or personal relationships that could have appeared to influence the work reported in this paper.

Acknowledgements

We thank Sehong Kang and Joo Hun Lee for their valuable discussion and assistance in revising the manuscript. SEM and Micro-CT imaging were conducted at the Microscopy Suite of the Beckman Institute at the University of Illinois at Urbana-Champaign. Confocal imaging was conducted at the Core Facilities of the Carl R. Woese Institute for Genomic Biology at the University of Illinois at Urbana-Champaign.

Appendix A. Supplementary data

Supplementary data to this article can be found online at https://doi.org/10.1016/j.biomaterials.2026.124131.

Data availability

Data will be made available on request.

References

[1] M.N.T. Le, M. Takahi, K. Maruyama, A. Kurisaki, K. Ohnuma, Cardiac differentiation at an initial low density of human-induced pluripotent stem cells, In Vitro Cell. Dev. Biol. Anim. 54 (2018) 513–522, https://doi.org/10.1007/s11626-018-0276-0.

[2] X. Lian, J. Zhang, S.M. Azarin, K. Zhu, L.B. Hazeltine, X. Bao, C. Hsiao, T.J. Kamp, S.P. Palecek, Directed cardiomyocyte differentiation from human pluripotent stem cells by modulating Wnt/β-catenin signaling under fully defined conditions, Nat. Protoc. 8 (2013) 162–175, https://doi.org/10.1038/nprot.2012.150.

[3] H. Kempf, R. Olmer, A. Haase, A. Franke, E. Bolesani, K. Schwanke, D. Robles-Diaz, M. Coffee, G. Göhring, G. Dräger, O. Pötz, T. Joos, E. Martinez-Hackert, A. Haverich, F.F.R. Buettner, U. Martin, R. Zweigerdt, Bulk cell density and Wnt/TGFbeta signalling regulate mesendodermal patterning of human pluripotent stem cells, Nat. Commun. 7 (2016) 13602, https://doi.org/10.1038/ncomms13602.

[4] S.J. Kim, E.M. Kim, M. Yamamoto, H. Park, H. Shin, Engineering multi-cellular spheroids for tissue engineering and regenerative medicine, Adv. Healthc. Mater. 9 (2020) e2000608, https://doi.org/10.1002/adhm.202000608.

[5] L. Drakhlis, S. Biswanath, C.M. Farr, V. Lupanow, J. Teske, K. Ritzenhoff, A. Franke, F. Manstein, E. Bolesani, H. Kempf, S. Liebscher, K. Schenke-Layland, J. Hegermann, L. Nolte, H. Meyer, J. de la Roche, S. Thiemann, C. Wahl-Schott, U. Martin, R. Zweigerdt, Human heart-forming organoids recapitulate early heart and foregut development, Nat. Biotechnol. 39 (2021) 737–746, https://doi.org/10.1038/s41587-021-00960-1.

[6] J. Lee, A. Sutani, R. Kaneko, J. Takeuchi, T. Sasano, T. Kohda, K. Ihara, K. Takahashi, M. Yamazoe, T. Morio, T. Furukawa, F. Ishino, *In Vitro* generation of functional murine heart organoids via FGF4 and extracellular matrix, Nat. Commun. 11 (2020) 4283, https://doi.org/10.1038/s41467-020-18031-5.

[7] R.J. Mills, D.M. Titmarsh, X. Koenig, B.L. Parker, J.G. Ryall, G.A. Quaife-Ryan, H. K. Voges, M.P. Hodson, C. Ferguson, L. Drowley, A.T. Plowright, E.J. Needham, Q. D. Wang, P. Gregorevic, M. Xin, W.G. Thomas, R.G. Parton, L.K. Nielsen, B. S. Launikonis, D.E. James, D.A. Elliott, E.R. Porrello, J.E. Hudson, Functional screening in human cardiac organoids reveals a metabolic mechanism for cardiomyocyte cell cycle arrest, Proc. Natl. Acad. Sci. U. S. A. 114 (2017) e8372–e8381, https://doi.org/10.1073/pnas.1707316114.

[8] R.J. Mills, S.J. Humphrey, P.R.J. Fortuna, M. Lor, S.R. Foster, G.A. Quaife-Ryan, R. L. Johnston, T. Dumenil, C. Bishop, R. Rudraraju, D.J. Rawle, T. Le, W. Zhao, L. Lee, C. Mackenzie-Kludas, N.R. Mehdiabadi, C. Halliday, D. Gilham, L. Fu, S. J. Nicholls, J. Johansson, M. Sweeney, N.C.W. Wong, E. Kulikowski, K. A. Sokolowski, B.W.C. Tse, L. Devilée, H.K. Voges, L.T. Reynolds, S. Krumeich, E. Mathieson, D. Abu-Bonsrah, K. Karavendzas, B. Griffen, D. Titmarsh, D.A. Elliott, J. McMahon, A. Suhrbier, K. Subbarao, E.R. Porrello, M.J. Smyth, C.R. Engwerda, K.P.A. MacDonald, T. Bald, D.E. James, J.E. Hudson, BET inhibition blocks inflammation-induced cardiac dysfunction and SARS-CoV-2 infection, Cell 184 (2021) 2167–2182.e2122, https://doi.org/10.1016/j.cell.2021.03.026.

[9] M.E. Kupfer, W.-H. Lin, V. Ravikumar, K. Qiu, L. Wang, L. Gao, D.B. Bhuiyan, M. Lenz, J. Ai, R.R. Mahutga, D. Townsend, J. Zhang, M.C. McAlpine, E. G. Tolkacheva, B.M. Ogle, *In Situ* expansion, differentiation, and electromechanical coupling of human cardiac muscle in a 3D bioprinted, chambered organoid, Circ. Res. 127 (2020) 207–224, https://doi.org/10.1161/CIRCRESAHA.119.316155.

[10] A. Pramanick, T. Hayes, V. Sergis, E. McEvoy, A. Pandit, A.C. Daly, 4D bioprinting shape-morphing tissues in granular support hydrogels: sculpting structure and guiding maturation, Adv. Funct. Mater. 35 (2025) 2414559, https://doi.org/10.1002/adfm.202414559.

[11] P. Hofbauer, S.M. Jahnel, N. Pápai, M. Giesshammer, A. Deyett, C. Schmidt, M. Penc, K. Tavernini, N. Grdseloff, C. Meledeth, L.C. Ginistrelli, C. Ctortecka, Š. Šalic, M. Novatchkova, S. Mendjan, Cardioids reveal self-organizing principles of human cardiogenesis, Cell 184 (2021) 3299–3317.e22, https://doi.org/10.1016/j.cell.2021.04.034.

[12] A. Harihara, K. Moshksayan, N. Momtahan, A. Ben-Yakar, J. Zoldan, Evaluating seeding density effects on cardiac organoid health and functionality for toxicity studies, Tissue Eng. Part A (2025) 19373341251392244, https://doi.org/10.1177/19373341251392244.

[13] C.H. Weimar, E.D. Post Uiterweer, G. Teklenburg, C.J. Heijnen, N.S. Macklon, Reprint of: in-Vitro model systems for the study of human embryo-endometrium interactions, Reprod. Biomed. Online 27 (2013) 673–688, https://doi.org/10.1016/j.rbmo.2013.08.002.

[14] P.J. van der Linden, Cell adhesion, cell adhesion molecules and their functional role in the human endometrium, Early Pregnancy 2 (1996) 5–14.

[15] E.A. Stewart, S.K. Laughlin-Tommaso, W.H. Catherino, S. Lalitkumar, D. Gupta, B. Vollenhoven, Uterine fibroids, Nat. Rev. Dis. Primers 2 (2016) 16043, https://doi.org/10.1038/nrdp.2016.43.

[16] T. Hiraoka, Y. Osuga, Y. Hirota, Current perspectives on endometrial receptivity: a comprehensive overview of etiology and treatment, J. Obstet. Gynaecol. Res. 49 (2023) 2397–2409, https://doi.org/10.1111/jog.15759.

[17] S.O. Sarrigiannidis, J.M. Rey, O. Dobre, C. González-García, M.J. Dalby, M. Salmeron-Sanchez, A tough act to follow: collagen hydrogel modifications to improve mechanical and growth factor loading capabilities, Mater. Today Bio 10 (2021) 100098, https://doi.org/10.1016/j.mtbio.2021.100098.

[18] N.E. Clay, K. Shin, A. Ozcelikkale, M.K. Lee, M.H. Rich, D.H. Kim, B. Han, H. Kong, Modulation of matrix softness and interstitial flow for 3D cell culture using a cell-microenvironment-on-a-chip system, ACS Biomater. Sci. Eng. 2 (2016) 1968–1975, https://doi.org/10.1021/acsbiomaterials.6b00379.

[19] W. Park, E.M. Kim, Y. Jeon, J. Lee, J. Yi, J. Jeong, B. Kim, B.G. Jeong, D.R. Kim, H. Kong, C.H. Lee, Transparent intracellular sensing platform with Si needles for simultaneous live imaging, ACS Nano 17 (2023) 25014–25026, https://doi.org/10.1021/acsnano.3c07527.

[20] B.B. O'Connor, B.D. Pope, M.M. Peters, C. Ris-Stalpers, K.K. Parker, The role of extracellular matrix in normal and pathological pregnancy: future applications of microphysiological systems in reproductive medicine, Exp. Biol. Med. (Maywood) 245 (2020) 1163–1174, https://doi.org/10.1177/1535370220938741.

[21] K.M. Sullivan, C.G. Park, J.D. Ito, M. Kandel, G. Popescu, Y.J. Kim, H. Kong, Matrix softness-mediated 3D zebrafish hepatocyte modulates response to endocrine disrupting chemicals, Environ. Sci. Technol. 54 (2020) 13797–13806, https://doi.org/10.1021/acs.est.0c01988.

[22] J. Xie, M. Bao, S.M.C. Bruekers, W.T.S. Huck, Collagen gels with different fibrillar microarchitectures elicit different cellular responses, ACS Appl. Mater. Interfaces 9 (2017) 19630–19637, https://doi.org/10.1021/acsami.7b03883.

[23] R.S. Navarro, M.S. Huang, J.G. Roth, K.M. Hubka, C.M. Long, A. Enejder, S. C. Heilshorn, Tuning polymer hydrophilicity to regulate gel mechanics and encapsulated cell morphology, Adv. Healthc. Mater. 11 (2022) e2200011, https://doi.org/10.1002/adhm.202200011.

[24] Y. Abbas, A. Carnicer-Lombarte, L. Gardner, J. Thomas, J.J. Brosens, A. Moffett, A. M. Sharkey, K. Franze, G.J. Burton, M.L. Oyen, Tissue stiffness at the human maternal-fetal interface, Hum. Reprod. 34 (2019) 1999–2008, https://doi.org/10.1093/humrep/dez139.

[25] X. Jiang, P. Asbach, K.-J. Streitberger, A. Thomas, B. Hamm, J. Braun, I. Sack, J. Guo, *In vivo* high-resolution magnetic resonance elastography of the uterine corpus and cervix, Eur. Radiol. 24 (2014), https://doi.org/10.1007/s00330-014-3305-8.

[26] M. Litviňuková, C. Talavera-López, H. Maatz, D. Reichart, C.L. Worth, E. L. Lindberg, M. Kanda, K. Polanski, M. Heinig, M. Lee, E.R. Nadelmann, K. Roberts, L. Tuck, E.S. Fasouli, D.M. DeLaughter, B. McDonough, H. Wakimoto, J. M. Gorham, S. Samari, K.T. Mahbubani, K. Saeb-Parsy, G. Patone, J.J. Boyle, H. Zhang, H. Zhang, A. Viveiros, G.Y. Oudit, O.A. Bayraktar, J.G. Seidman, C. E. Seidman, M. Noseda, N. Hubner, S.A. Teichmann, Cells of the adult human heart, Nature 588 (2020) 466–472, https://doi.org/10.1038/s41586-020-2797-4.

[27] C.P. Hsu, B. Moghadaszadeh, J.H. Hartwig, A.H. Beggs, Sarcomeric and nonmuscle α-actinin isoforms exhibit differential dynamics at skeletal muscle Z-lines, Cytoskeleton (Hoboken) 75 (2018) 213–228, https://doi.org/10.1002/cm.21442.

[28] M.A. Skylar-Scott, S.G.M. Uzel, L.L. Nam, J.H. Ahrens, R.L. Truby, S. Damaraju, J. A. Lewis, Biomanufacturing of organ-specific tissues with high cellular density and embedded vascular channels, Sci. Adv. 5 (2019), https://doi.org/10.1126/sciadv.aaw2459 eaaw2459.

[29] M. Baruscotti, A. Bucchi, C. Viscomi, G. Mandelli, G. Consalez, T. Gnecchi-Rusconi, N. Montano, K.R. Casali, S. Micheloni, A. Barbuti, D. DiFrancesco, Deep bradycardia and heart block caused by inducible cardiac-specific knockout of the pacemaker channel gene Hcn4, Proc. Natl. Acad. Sci. U. S. A. 108 (2011) 1705–1710, https://doi.org/10.1073/pnas.1010122108.

[30] M.L. Schulze, M.D. Lemoine, A.W. Fischer, K. Scherschel, R. David, K. Riecken, A. Hansen, T. Eschenhagen, B.M. Ulmer, Dissecting hiPSC-CM pacemaker function in a cardiac organoid model, Biomaterials 206 (2019) 133–145, https://doi.org/10.1016/j.biomaterials.2019.03.023.

[31] M.J. Betzenhauser, G.S. Pitt, C. Antzelevitch, Calcium channel mutations in cardiac arrhythmia syndromes, Curr. Mol. Pharmacol. 8 (2015) 133–142, https://doi.org/10.2174/1874467208666150518114857.

[32] G.L. Guo, L.Q. Sun, M.H. Sun, H.M. Xu, LncRNA SLC8A1-AS1 protects against myocardial damage through activation of cGMP-PKG signaling pathway by inhibiting SLC8A1 in mice models of myocardial infarction, J. Cell. Physiol. 234 (2019) 9019–9032, https://doi.org/10.1002/jcp.27574.

[33] C.M.J. Tan, A.J. Lewandowski, The transitional heart: from early embryonic and fetal development to neonatal life. *Fetal. Diagn*, Ther. 47 (2020) 373–386, https://doi.org/10.1159/000501906.

[34] K. Nishii, Y. Shibata, Mode and determination of the initial contraction stage in the mouse embryo heart, Anat. Embryol. 211 (2006) 95–100, https://doi.org/10.1007/s00429-005-0065-x.

[35] R.C.V. Tyser, A.M.A. Miranda, C.-M. Chen, S.M. Davidson, S. Srinivas, P.R. Riley, Calcium handling precedes cardiac differentiation to initiate the first heartbeat, eLife 5 (2016) e17113, https://doi.org/10.7554/eLife.17113.

[36] Y.R. Lewis-Israeli, A.H. Wasserman, M.A. Gabalski, B.D. Volmert, Y. Ming, K. A. Ball, W. Yang, J. Zou, G. Ni, N. Pajares, X. Chatzistavrou, W. Li, C. Zhou, A. Aguirre, Self-assembling human heart organoids for the modeling of cardiac development and congenital heart disease, Nat. Commun. 12 (2021) 5142, https://doi.org/10.1038/s41467-021-25329-5.

[37] O.M. Martínez-Estrada, L.A. Lettice, A. Essafi, J.A. Guadix, J. Slight, V. Velecela, E. Hall, J. Reichmann, P.S. Devenney, P. Hohenstein, N. Hosen, R.E. Hill, R. Muñoz-Chapuli, N.D. Hastie, Wt1 is required for cardiovascular progenitor cell formation through transcriptional control of Snail and E-cadherin, Nat. Genet. 42 (2010) 89–93, https://doi.org/10.1038/ng.494.

[38] S.J. Conway, Novel expression of the goosecoid transcription factor in the embryonic mouse heart, Mech. Dev. 81 (1999) 187–191, https://doi.org/10.1016/s0925-4773(98)00235-4.

[39] K. Togi, T. Kawamoto, R. Yamauchi, Y. Yoshida, T. Kita, M. Tanaka, Role of Hand1/eHAND in the dorso-ventral patterning and interventricular septum formation in the embryonic heart, Mol. Cell Biol. 24 (2004) 4627–4635, https://doi.org/10.1128/mcb.24.11.4627-4635.2004.

[40] S.J. Serrano-Gomez, M. Maziveyi, S.K. Alahari, Regulation of epithelial-mesenchymal transition through epigenetic and post-translational modifications, Mol. Cancer 15 (2016) 18, https://doi.org/10.1186/s12943-016-0502-x.

[41] A. Standish, L.W. Enquist, J.S. Schwaber, Innervation of the heart and its central medullary origin defined by viral tracing, Science 263 (1994) 232–234, https://doi.org/10.1126/science.8284675.

[42] P.C. Béguin, V. El-Helou, M.A. Gillis, N. Duquette, H. Gosselin, R. Brugada, L. Villeneuve, D. Lauzier, J.F. Tanguay, C. Ribuot, A. Calderone, Nestin$^{(+)}$ stem cells independently contribute to neural remodelling of the ischemic heart, J. Cell. Physiol. 226 (2011) 1157–1165, https://doi.org/10.1002/jcp.22441.

[43] K. Kimura, M. Ieda, H. Kanazawa, T. Yagi, M. Tsunoda, S. Ninomiya, H. Kurosawa, K. Yoshimi, H. Mochizuki, K. Yamazaki, S. Ogawa, K. Fukuda, Cardiac sympathetic rejuvenation: a link between nerve function and cardiac hypertrophy, Circ. Res. 100 (2007) 1755–1764, https://doi.org/10.1161/01.RES.0000269828.62250, ab.

[44] A.D. Doyle, Fluorescent labeling of rat-tail collagen for 3D fluorescence imaging, Bio. Protoc. 8 (2018) e2919, https://doi.org/10.21769/BioProtoc.2919.

[45] K. Coutu, A.N. Sangwa, N. Gaudreault, S.S. Tayebi, T. Hoare, P. Mhaskar, N. Bertrand, A.A. Greschner, M.A. Gauthier, Direct quantification of PEGylation for intact bioconjugates and nanoparticles by the colorimetric Barium/Iodide assay, Biomacromolecules 26 (2025) 3689–3699, https://doi.org/10.1021/acs.biomac.5c00274.

[46] Liang, T.W. Jensen, E.J. Roy, C. Cha, R.J. Devolder, R.E. Kohman, B.Z. Zhang, K. B. Textor, L.A. Rund, L.B. Schook, Y.W. Tong, H. Kong, Tuning the non-equilibrium state of a drug-encapsulated poly(ethylene glycol) hydrogel for stem and progenitor cell mobilization, Biomaterials 32 (2011) 2004–2012, https://doi.org/10.1016/j.biomaterials.2010.11.021.

[47] H. Kim, M.K. Kim, H. Jang, B. Kim, D.R. Kim, C.H. Lee, Sensor-instrumented scaffold integrated with microporous spongelike ultrabuoy for long-term 3D mapping of cellular behaviors and functions, ACS Nano 13 (2019) 7898–7904, https://doi.org/10.1021/acsnano.9b02291.